A core in a star-forming disc as evidence of inside-out growth in the early Universe
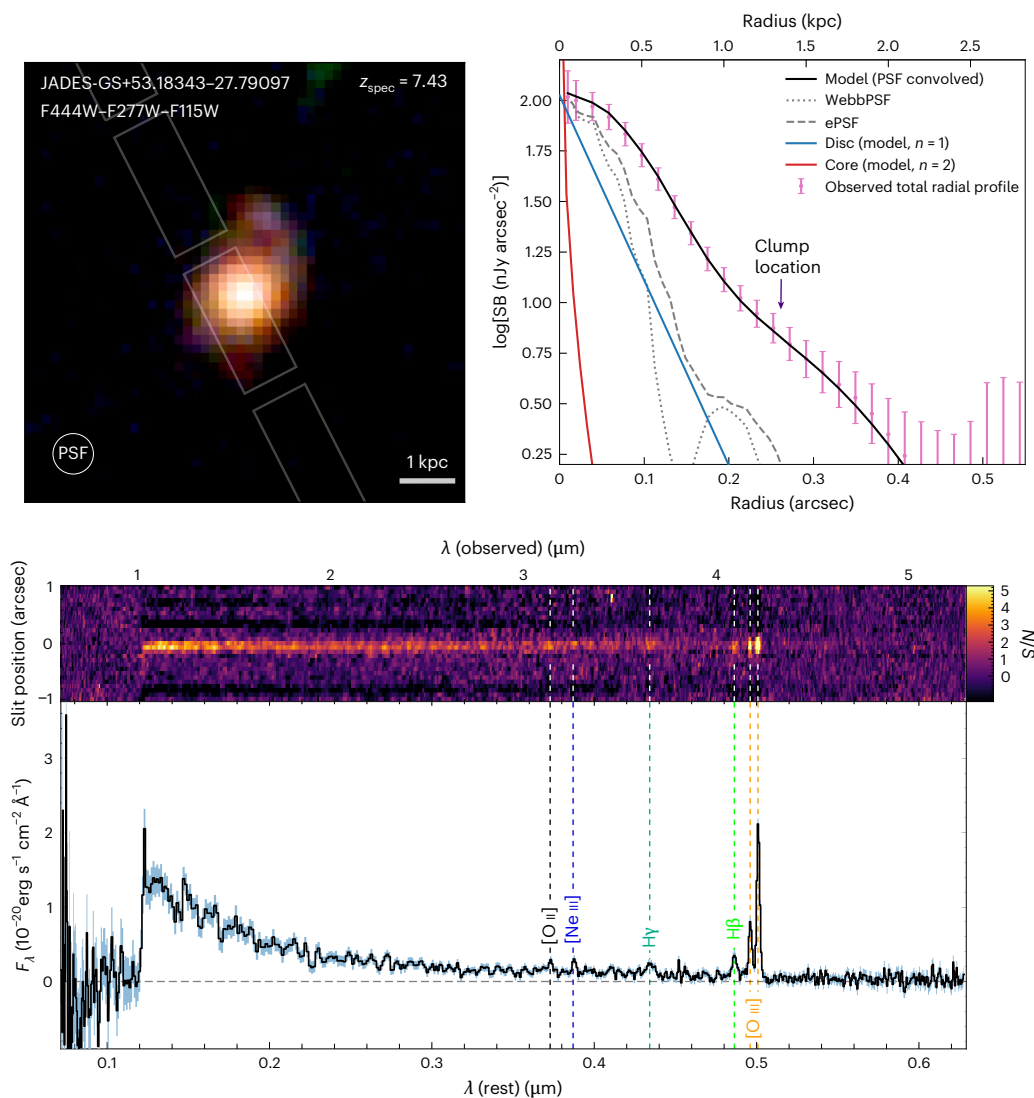
William M. Baker [1,2] ✉, Sandro Tacchella [1,2] ✉, Benjamin D. Johnson [3], Erica Nelson [4], Katherine A. Suess [5,6], Francesco D'Eugenio[1,2], Mirko Curti [1,2,7], Anna de Graaff [8], Zhiyuan Ji[9], Roberto Maiolino [1,2,10], Brant Robertson [5], Jan Scholtz[1,2], Stacey Alberts[9], Santiago Arribas [11], Kristan Boyett [12,13], Andrew J. Bunker [14], Stefano Carniani [15], Stephane Charlot [16], Zuyi Chen [9], Jacopo Chevallard[14], Emma Curtis-Lake [17], A. Lola Danhaive[1,2], Christa DeCoursey[9], Eiichi Egami [9], Daniel J. Eisenstein [3], Ryan Endsley[18], Ryan Hausen [19], Jakob M. Helton [9], Nimisha Kumari [20], Tobias J. Looser [1,2], Michael V. Maseda [21], Dávid Puskás [1,2], Marcia Rieke[9], Lester Sandles[1,2], Fengwu Sun[9], Hannah Übler [1,2], Christina C. Williams [22], Christopher N. A. Willmer [9] & Joris Witstok[1,2]

The physical processes that establish the morphological evolution and the structural diversity of galaxies are key unknowns in extragalactic astrophysics. Here we report the finding of the morphologically mature galaxy JADES-GS+53.18343−27.79097, which existed within the first 700 million years of the Universe's history. This star-forming galaxy with a stellar mass of 400 million solar masses consists of three components: a highly compact core with a half-light radius of less than 100 pc, an actively star-forming disc with a radius of about 400 pc and a star-forming clump, all of which show distinctive star-formation histories. The central stellar mass density of this galaxy is within a factor of 2 of the most massive present-day ellipticals, while being globally 1,000 times less massive. The radial profile of the specific star-formation rate is rising towards the outskirts. This evidence suggests a detection of the inside-out growth of a galaxy as a proto-bulge and a star-forming disc in the epoch of reionization.

In the hierarchical Λ cold dark matter cosmological model (where Λ is a term equivalent to a cosmological constant), galaxies sustain their star formation for extended periods of time in a quasi-steady state of gas inflow, gas outflow and gas consumption[1,2]. To first order, the gas that cools at later cosmic epochs has higher angular momentum; therefore, it settles in a more extended star-forming disc, implying that galaxies grow from the inside out[3,4]. However, the actual formation of galaxies in the cosmological context is more complex as a wide range of processes regulate star formation and the orbital distribution of stars, ranging from stellar feedback (from supernovae and stellar winds), black hole feedback and cosmic rays, to galaxy–galaxy interactions and mergers[5–9].

Therefore, the morphological structure and spatially resolved growth rates of galaxies are a sensitive—but also complicated—probe of galaxy formation physics[10–16].

Galaxies in the local Universe show a range of morphologies, from younger disc-dominated spiral galaxies to older bulge-dominated ellipticals[17,18], and are typically classified by the Hubble sequence[19–21]. The growth of local star-forming galaxies has been observed on spatially resolved scales, confirming that in general galaxies grow inside-out[22–24]. However, there is a diverse range of specific star-formation rate (sSFR) profiles in the local universe with some galaxies undergoing inside-out growth, while others grow outside-in[25–27], probably corresponding to

A full list of affiliations appears at the end of the paper. ✉e-mail: wb308@cam.ac.uk; st578@cam.ac.uk

Fig. 1 | NIRCam imaging and NIRSpec spectroscopic data of the galaxy. Top left: the (F444W–F277W–F115W) colour-composite image of the galaxy, where the central core and disc are prominent. A 1 kpc scale bar (corresponding to 0.19 arcsec), the F444W PSF and the position of the NIRSpec slit are overplotted. Top right: the total radial (azimuthally averaged) surface brightness (SB) profile of the core, disc and clump in the F356W band, where the pink points are the observational data and the black line is the PSF-convolved best-fit three-component model (consisting of the core, disc and clump). The error bars correspond to the error propagated through from the error maps (that is, the standard deviation). The intrinsic best-fit Sérsic profiles of the core and disc components are shown as red and blue lines, respectively. The off-centred clump at a distance of 1.4 kpc is indicated with a purple arrow. The grey dashed and dotted lines correspond to the ePSF and the WebbPSF, respectively, in the F356W band. Bottom: the two-dimensional and one-dimensional NIRSpec R100 prism spectra, with the position of notable detected emission lines overplotted, which indicates that this galaxy is dominated by stellar emission. The two-dimensional spectrum includes the slit position and the colour bar corresponds to the signal-to-noise ratio (S/N). The one-dimensional spectrum shows flux against rest-frame wavelength. The errors on the one-dimensional spectrum correspond to the standard deviation of the mean signal.

different growth phases. Most of the mass of local galaxies is found to have formed during the redshift range $1 \lesssim z \lesssim 3$, around the period of 'cosmic noon', the peak of the cosmic star-formation rate (SFR) density in the Universe[28]. Observations at these redshifts have revealed many galaxies with massive bulges and rotating discs[25,29–31]. However, to probe the build-up of these $1 \lesssim z \lesssim 3$ bulges, we need to investigate even earlier cosmic times, characterizing galaxies during the epoch of reionization ($z \gtrsim 6$)[32]. Observationally, little is known about how quickly these early galaxies grow, in particular on spatially resolved scales. The theoretical expectation is that the galaxy merger rate increases towards higher redshifts[33–35], which could lead to more pronounced central starbursts[36,37]. Recent numerical models indicate that early (at $z > 3$), low-mass ($10^{7-9} M_\odot$) galaxies can undergo rapid size fluctuations and compaction driven by the competition between feedback-driven gas outflows and cold inflows[38,39], leading to a flat or even inverted size–mass relation with more massive galaxies being smaller ($<10^9 M_\odot$). Direct observations will address questions about how galaxies grow their stellar mass and size in the early Universe, thereby providing insights into the physics that regulates star formation.

The James Webb Space Telescope (JWST) opens a new window to study the formation of the Hubble sequence and bulge–disc formation in the early Universe[40–42]. As part of the JWST Advanced Deep Extragalactic Survey (JADES)[43–45], we report here the discovery of a core–disc galaxy with an off-centre clump (JADES-GS+53.18343−27.79097) at a spectroscopic redshift of 7.430 (Methods), when the Universe was only 700 Myr old. JADES-GS+53.18343−27.79097 appears to be growing inside-out, having built up a massive compact core at its centre before forming a surrounding star-forming disc. Here we are able to characterize a core–disc system during the epoch of reionization and find the signature of early bulge formation.

Table 1 | Key stellar population and morphological properties of the core, disc and clump components

	$\log(M_\star/M_\odot)$	t_{half} (Myr)	SFR_{10Myr} ($M_\odot\,yr^{-1}$)	SFR_{100Myr} ($M_\odot\,yr^{-1}$)	$\log(Z/Z_\odot)$	A_V	n	r_e (mas)
Disc	$7.98^{+0.25}_{-0.19}$	19^{+108}_{-15}	$4.8^{+0.7}_{-0.6}$	$0.7^{+0.3}_{-0.2}$	$-1.5^{+0.5}_{-0.3}$	$0.08^{+0.05}_{-0.03}$	1.0^a	80^{+16}_{-16}
Core	$8.38^{+0.18}_{-0.16}$	68^{+78}_{-31}	$1.0^{+0.8}_{-0.7}$	$1.7^{+0.8}_{-0.7}$	$-1.7^{+0.4}_{-0.2}$	$0.02^{+0.07}_{-0.02}$	$2.03^{+0.3}_{-0.3}$	16^{+3}_{-3}
Clump	$7.22^{+0.42}_{-0.22}$	44^{+146}_{-38}	$0.5^{+0.2}_{-0.1}$	$0.1^{+0.1}_{-0.0}$	$-1.3^{+0.7}_{-0.4}$	$0.13^{+0.09}_{-0.06}$	1.0^a	5^{+0}_{-0}

From left to right, stellar mass, half-time (the half-mass assembly time), SFR averaged over 10 Myr, SFR averaged over 100 Myr, stellar metallicity, extinction in the V band A_V, Sérsic index n and half-light radius r_e. ^{a}The Sérsic index of the disc and clump are fixed to $n=1$.

Core−disc−clump decomposition

We use Near-Infrared Camera (NIRCam)[46] imaging in nine filters (F090W, F115W, F150W, F200W, F277W, F335M, F356W, F410M and F444W) and Near-Infrared Spectrograph (NIRSpec) micro-shutter array (MSA)[47–49] spectroscopy from JADES in the Great Observatories Origins Deep Survey-South (GOODS-S) region[50]. This gives us extended coverage of the rest-frame ultraviolet and optical wavelengths (including the Balmer break), which constrains the stellar populations on spatially resolved scales. Furthermore, the medium band F410M probes the strength of the emission lines Hβ + [O III] on spatially resolved scales.

The top-left panel of Fig. 1 shows a colour-composite red–green–blue (RGB, corresponding to F444W–F277W–F115W) image of JADES-GS+53.18343−27.79097. The image shows a compact central component (core) surrounded by an extended, disc-like component. JADES-GS+53.18343−27.79097 has a strong colour gradient between the central region and the outskirts (Extended Data Fig. 6), implying an excess of Hβ + [O III] in the outskirts as probed by F410M. To quantify the compactness and colour gradient, we employ the tool ForcePho (B.D.J., manuscript in preparation) to perform a detailed morphological and photometric analysis of JADES-GS+53.18343−27.79097, forward modelling all individual exposures across all bands simultaneously and accounting for the point-spread functions (PSFs; see 'Morphology and photometry with ForcePho' in Methods). We explore a range of different models and find that a three-component model, consisting of a disc Sérsic profile (fixing the Sérsic index to $n=1$ by limiting the bounds to ±0.01), a compact component ($n=2$–5) consistent with a bulge or pseudobulge, and an off-centre clump (modelled as a quasi-point source), reproduces the data best (with the smallest residuals and χ^2). Although this model is not unique, it is able to capture the complex morphology of this galaxy in all of the filters. We obtain a central core with a half-light radius of 16 mas (roughly 80 pc), while the disc has a half-light radius of 80 mas (about 400 pc; Table 1), overall confirming the compact nature of the source. Although we refer to the extended component as a 'disc' from a purely morphological perspective, the ionized gas (as traced by F410M) of JADES-GS+53.18343−27.79097 is actually consistent with a rotationally supported component with a velocity at the effective radius divided by velocity dispersion of $v(r_{eff})/\sigma_0 \approx 1.3$ (ref. 51).

Figure 1, top right, shows the surface brightness profile of the galaxy in the F356W band, the best-fit model convolved with the PSF (black), the unconvolved Sérsic model components (core in red and disc in blue), and the WebbPSF and empirical PSF (ePSF) of the mosaic (grey dotted and dashed line). This shows that the PSF-convolved three-component model reproduces the observed surface brightness profile (see 'Motivation for the multiple-component fit' in Methods for a detailed plot of the model and residual). We also fit a single-component model with and without the clump, plus just a core + disc fit, all of which we test against our fiducial three-component model. We find that all of these model variants fail to account for either the additional flux in the centre and/or the flux of the clump, resulting in higher χ^2 statistic values (0.45, 0.25 and 0.18 versus 0.14 for the fiducial three-component fit; see 'Motivation for the multiple-component fit' in Methods). We also calculate a reduced χ^2 that favours the fiducial three-component model. To check against PSF-approximation issues with ForcePho, we re-simulate the core, disc and clump fits convolved with the WebbPSF,

and then refit them. Using the WebbPSF model, we find that the results are consistent with the original fit within the uncertainties, confirming that the ForcePho PSF approximations are appropriate (see 'PSF approximations in ForcePho' in Methods).

Figure 1, bottom, shows the two-dimensional and one-dimensional NIRSpec R100 prism spectra of JADES-GS+53.18343−27.79097, including the positions of notable detected emission lines. This spectrum probes both the core and the disc, as indicated by the slit position in the top-left panel of Fig. 1. Using these data, we estimate a spectroscopic redshift of $z_{spec}=7.430$, consistent with the photometric redshift. The measured emission-line fluxes from the NIRSpec prism spectrum indicate that this galaxy is consistent with stellar emission, and the high-resolution grating spectrum shows that all emission lines (in particular Hβ) are narrow, implying that this galaxy does not appear to host a dominant active galactic nucleus (AGN; see 'Star formation versus AGN' in Methods), but we note that it is difficult to fully rule out an AGN.

Stellar population properties

In Fig. 2, we show the ForcePho-based spectral energy distributions (SEDs) of the core, disc and clump components. To explore the stellar population properties of the three components, we fit the individual SEDs using the Bayesian SED-fitting tool Prospector[52]. We input the flux values and errors obtained for each band from ForcePho, and independently fit the SEDs with a flexible star-formation history (SFH) with the standard continuity prior[53], a variable dust attenuation law with a free dust attenuation law index and normalization, and a nebular emission model. We also test using a bursty-continuity prior for the SFH, finding that we obtain stellar masses consistent with the standard continuity prior (see 'SED fitting with Prospector' in Methods). In Fig. 2, we plot the best fit for the SEDs of the three components, indicating that the SEDs are well reproduced by stellar emission in conjunction with dust attenuation and nebular emission.

Table 1 gives the key stellar population properties of the core, disc and clump components. The core is the most massive of the components with a stellar mass (in units of solar masses) of $\log(M_\star/M_\odot)=8.4^{+0.2}_{-0.2}$, while the disc has $\log(M_\star/M_\odot)=8.0^{+0.3}_{-0.2}$, despite the core having a radius (~80 pc) less than a quarter of that of the disc (~400 pc). This suggests that the core is dense (stellar mass surface density of $\Sigma_{eff}=\frac{M_\star}{2\pi r^2}\approx 6\times10^9\,M_\odot\,kpc^{-2}$). The bottom-right panel of Fig. 2 shows the SFR as a function of lookback time for the core (red), the disc (blue) and the clump (purple). These SFHs show the full posterior distributions, that is, they take into account the degeneracies with other parameters, such as the dust attenuation law. The core, disc and clump have varying SFHs, with the core undergoing an earlier period of star formation with a recent decline, while the disc is currently undergoing a burst of star formation. Consistently, the stellar age (lookback time when half of the stellar mass formed) for the core is rather old with $t_{half}=68^{+78}_{-31}$ Myr , while the disc is younger ($t_{half}=19^{+108}_{-15}$ Myr). In total, we find that the combined core + disc galaxy has a stellar mass of $\log(M_\star/M_\odot)=8.5^{+0.2}_{-0.2}$ and star-formation rate $SFR_{10Myr}=5.8^{+1.5}_{-1.3}\,M_\odot\,yr^{-1}$, giving it an sSFR of $\log(sSFR\,yr^{-1})=-7.7^{+0.1}_{-0.1}$ (typical for $7\le z\le 8$ galaxies[54]). For comparison, from the NIRSpec spectrum we derive a dust-corrected Hβ SFR
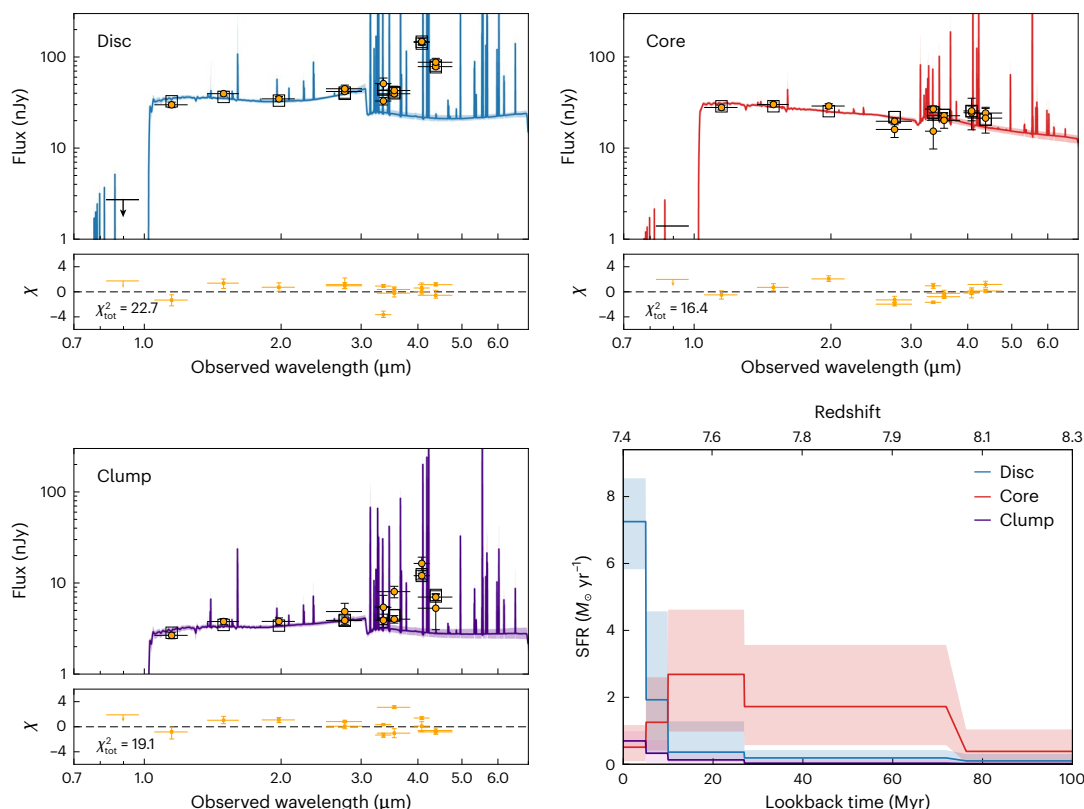
Fig. 2 | SEDs for the three components and their SFHs. SED fits for the disc (top left), core (top right), and clump (bottom left) components. The yellow points show the photometry inferred from the ForcePho modelling, while the 2σ upper limits are indicated as downward pointing arrows. The errors on the photometry are the 1σ uncertainties (which are derived via standard error propagation through the reduction pipeline). The errors on the x axis correspond to the widths of the filters. The open squares mark the photometry of the best-fit SED model. The solid lines and the shaded regions show the median and the

16th–84th percentiles of the SED posterior from the Prospector modelling. Bottom right: SFR against lookback time (from the observed redshift) for the disc (blue line), core (red line) and clump (purple line). The shading corresponds to the 16th and 84th percentiles of the SFH posterior. We find that the disc has been undergoing a burst of star formation for the past 5 Myr, while the core is entering a lower-star-formation phase. The clump has a lower SFR compared with the other two components and is over an order of magnitude less massive than the core.

of $SFR_{H\beta} = 9^{+30}_{-7}\,M_\odot\,yr^{-1}$, which is consistent with our SED-derived SFR over 10 Myr. We find a similar agreement for dust attenuation (Balmer decrement) and gas-phase metallicity between the SED-derived and NIRSpec-derived values (see 'Emission-line properties' in Methods). Although the clump is not the focus of this study, we find it to be low in stellar mass ($\log(M_\star/M_\odot) = 7.2^{+0.4}_{-0.2}$) and highly star-forming with an sSFR of $\log(sSFR\,yr^{-1}) = -7.5^{+0.3}_{-0.4}$ averaged over 10 Myr. The clump's age appears to be relatively unconstrained ($t_{half} = 44^{+146}_{-38}$ Myr), meaning that it could be young and have been formed through a disc instability, or—alternatively—it could be older and be an accreted satellite galaxy.

In summary, we find that the core and disc are similarly bright in the rest-ultraviolet and that the disc is dominating the most recent star formation and is slightly dust attenuated. This is surprising in the $z \approx 2$ picture of a red dusty bulge embedded in a blue disc with lower dust attenuation, but consistent with recent JWST observations showing populations of red dusty discs missed in previous rest-optically selected samples[55]. The observational data that drive this result are the higher F410M excess in the disc (Extended Data Fig. 6), which implies strong nebular line contribution and is consistent with inside-out growth. This is a good showcase of the power of medium-band observations to constrain stellar populations[56].
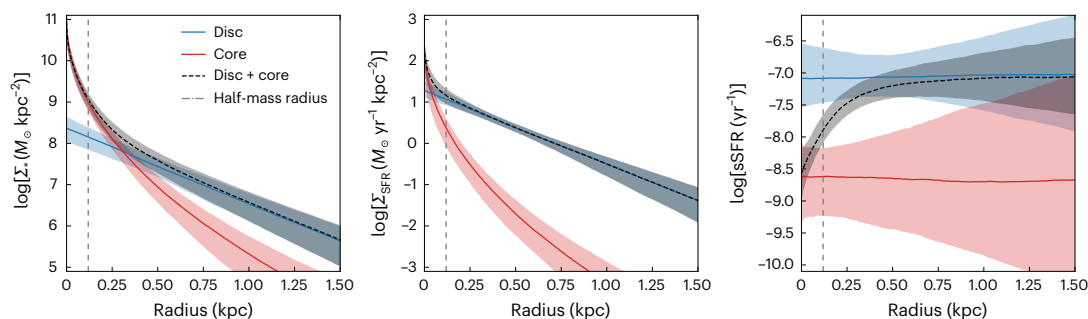
Radial profiles of stellar mass and star formation

The compact size and the medium-band excess with increasing radius (probing the youngest stars via nebular emission) are indicative of a

high central stellar mass density with a star-forming outskirt. We now use our multi-wavelength morphological decomposition and stellar population modelling to derive the intrinsic radial profiles of the stellar mass and SFR surface density. We use the unconvolved best-fit Sérsic profiles, normalized to the best-fit stellar mass and SFR for each component, as given (for example) for the stellar mass surface density profile by $\Sigma_\star(r) = \frac{M_\star\,I(r)}{I_{tot}}$, where $I(r)$ is the intensity inferred from the Sérsic profile at radius r and $I_{tot} = \int 2\pi\,I(r)r\,dr$. The assumption is that each component has a negligible radial gradient in their stellar populations. However, as the normalization of the individual components vary as a function of wavelength, we are able to account for stellar population gradients across the galaxy.

Figure 3 shows the stellar mass surface density ($\Sigma_\star$, left panel), the SFR surface density (Σ_{SFR}, middle panel) and the sSFR (right panel) against the radius for the core and disc components and the combined profile. The Σ_{SFR} profile shows how the disc completely dominates the profile compared with the core, while the $\Sigma_\star$ profile shows that the core's stellar mass surface density is prominent in the inner regions. We indicate in each diagram as a vertical dot-dashed grey line the half-mass radius ($R_\star = 126^{+37}_{-26}$ pc), which is the radius of the galaxy at which half the (core + disc) stellar mass is contained.

By construction, because they have the same Sérsic profile (that is, shape) for the SFR and stellar mass radial profiles, the sSFR ($= SFR/M_\star$) profiles are radially constant for the individual disc and core components, while their combined sSFR profile increases with radius as $sSFR(r) = \frac{\Sigma_{SFR,core} + \Sigma_{SFR,disc}}{\Sigma_{\star,core} + \Sigma_{\star,disc}}$. The sSFR profile shows where

Fig. 3 | Radial surface density profiles of stellar mass and star formation.
Radial profiles of stellar mass surface density ($\Sigma_\star$; left), SFR surface density (Σ_{SFR}; middle) and sSFR (right) for the core (solid red lines), disc (solid blue lines) and the combination of the two (dashed black lines). The shaded regions show the 16th and 84th percentile uncertainties from both the SED fitting and the structural measurements. The half-mass radius at the time of observation is overplotted as a vertical dashed-dotted line. This figure shows that the SFR surface density of the galaxy is, at almost all radii, completely dominated by the star-forming disc, while the stellar mass surface density in the central regions is dominated by the core. The sSFR increases with radius, implying that this galaxy grows from the inside out.

the galaxy grows, the stellar mass doubling timescale is approximately equal to 1/sSFR. We see that the sSFR is steeply increasing at the half-mass radius (about 1.5 dex within the central 1 kpc): the central 100 pc has a stellar mass doubling time of about 100 Myr, while the outskirt has a mass doubling timescale of about 10 Myr. This implies that this galaxy increases its half-mass radius with time and grows inside-out.

Discussion

We now compare our $z = 7.43$ galaxy with galaxies and stellar systems at lower redshift, which allows us to gain a complementary view on the spatially resolved growth from the stellar mass and SFR distribution. Figure 4 shows the effective stellar mass density (Σ_{eff}) and the half-mass radius as a function of the stellar mass for the core, disc and the combination of both components. We compare our measurements to the ones from ref. 57 of star-forming galaxies (SFGs) and quiescent galaxies (QGs) at $z = 2.0$–2.5 and from ref. 58, which contains data on local globular clusters (GCs), ultracompact dwarfs (UCDs) and compact ellipticals (cEs). In the right panel, we also plot the extrapolated growth of the half-mass radius from redshift 7.43 to redshift 1, assuming the SFR profile from Fig. 3.

Although our $z = 7.43$ galaxy has a lower stellar masses than the plotted SFGs and QGs at $z \approx 2$, Σ_{eff} lies in the upper envelope of $z \approx 2$ SFGs and in the range of QGs. Looking at the half-mass radius, we find that both size and stellar mass are not probed by $z \approx 2$ observations. To facilitate a comparison and gain insight into the formation of QGs at cosmic noon ($z = 1$–3), we grow the observed stellar mass profile according to two simple recipes: (1) at a constant SFR with the observed SFR profile (green line in Fig. 4); and (2) at a constant SFR but with the assumption that the scale length of the SFR surface density profile scales as $R_s \propto \frac{1}{(1+z)}$ (motivated by inside-out growth models[4]; orange line). We assume that the global SFR is constant because the decline of the star-forming main sequence and the higher SFR due to an increased stellar mass (on the star-forming main sequence) roughly cancel each other out. Although both scenarios are simplistic, both tracks naturally intersect with the $z \approx 2$ size–mass relation of QGs by $z \approx 1$–3, highlighting that our $z = 7.43$ galaxy is a natural progenitor of the QG population at $z \approx 2$.

We also consider how our $z = 7.43$ galaxy compares with local, $z = 0$ stellar systems. From the left panel in Fig. 4, we can see that this galaxy lies above Σ_{eff} of local GCs and UCD, but is comparable to low-mass ellipticals. This can also be seen from Fig. 5, which shows the stellar mass surface density ($\Sigma_\star$) as a function of radius. For comparison, we also plot the profiles of local analogues, UCDs, cEs, ellipticals with a cusp, and ellipticals with a core from the compilation gathered in

ref. 59. The profile for JADES-GS+53.18343−27.79097 is similar to that of cEs and more extended than that of UCDs. Interestingly, the central ($R < 20$ pc) density of our $z = 7.43$ galaxy is within 0.2 dex of those of massive elliptical galaxies seen in the Universe today, but we note that it contains just 0.1% of the total stellar mass of these galaxies. Specifically, this $z = 7.43$ galaxy has a stellar mass density at $R = 1$ kpc of $\Sigma_{\star,1kpc} = 6.6\,M_\odot$ kpc^{-2}, while the massive core ellipticals have on average $\Sigma_{\star,1kpc} = 9.4\,M_\odot$ kpc^{-2}, which is a difference of 2.8 orders of magnitude. If this galaxy evolves into such a massive elliptical by $z = 0$, we conclude that inside-out growth takes place in two phases: first as a star-forming galaxy, which we directly observe here, and then, second, as a QG from $z \approx 1$–3 to $z = 0$ via mergers that build up a stellar envelope[60,61].

How can a $z = 7.43$ galaxy build such a high central stellar mass density that is comparable to local ellipticals? Our analysis shows that the star-formation activity is dominated by the disc component. However, it is not clear whether there was an episode of disc formation before the peak of the SFH of the core (that is, more than 100 Myr ago): earlier disc formation is still a possibility based on the posterior distribution of the SFH (Extended Data Fig. 7). Therefore, we speculate that the following two scenarios are possible to build up this core. The first is continuous inside-out growth, where early disc formation took place in a extremely compact disc, forming the currently observed core[4]. Indeed, such compact disc-shaped objects have been observed at a redshift of more than 10 (ref. 44). An alternative is that the disc was formed first and suffered an infall of gas into the centre due to compaction[8,62], which then formed the core. The disc would then re-form via newly accreted gas.

Importantly, all stellar systems, including our galaxy at $z = 7.43$, are well below the maximum stellar surface density of $\Sigma_{max} = 10^{11.5}\,M_\odot$ kpc^{-2}. This universal maximum stellar surface density of dense stellar systems is a natural consequence of feedback-regulated star-formation physics[59,63].

Regarding the two inferred evolutionary tracks, we find that the constant Σ_{SFR} grows the galaxy efficiently within 1 kpc, leading to a profile at $z = 2$ that overpredicts the stellar mass density of local ellipticals in the central 300 pc and is comparable to Σ_{max} at $R < 10$ pc. However, the track where we scale the scale length of the SFR density has a lower $\Sigma_\star$ (that is, it does not violate Σ_{max}) and is more consistent with the one of massive elliptical profiles up to $R \approx 3$ kpc. We conclude that the inside-out growing model is more consistent with the low-redshift ellipticals.

In summary, our finding of JADES-GS+53.18343−27.79097, a core–disc galaxy with a star-forming clump during the epoch of reionization provides evidence for inside-out growth during the first 700 Myr of the Universe. This galaxy appears to be a potential candidate progenitor of a typical QG at redshift 2 and a present-day elliptical galaxy. This suggests that bulge formation can start at very early epochs and
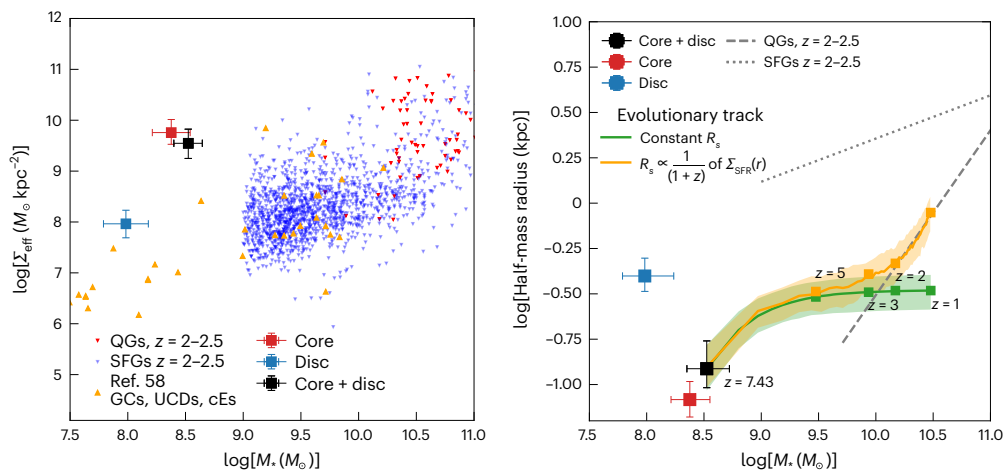
Fig. 4 | Stellar mass density and half-mass size in the context of lower-redshift galaxies. Left: effective stellar mass density (Σ_{eff}) versus stellar mass for the core (red square), disc (blue square) and the combination of both components (black square). The data are presented as the median of the distribution with errors corresponding to the 16th and 84th percentiles. We compare this with measurements from $z \approx 2$ (ref. 57) and $z = 0$ (ref. 58). Although our $z = 7.43$ galaxy is low in stellar mass, Σ_{eff} lies in the upper envelope of $z \approx 2$ SFGs and in the range of QGs. Right: half-mass size versus stellar mass for the core (red square), disc (blue square) and the combination of both components (black square). The

errors correspond to the 16th and 84th percentiles of the resulting distribution. The dotted and dashed lines show the size–mass relation at redshift $z \approx 2$ (ref. 57) for SFGs and QGs, respectively. The solid green line marks the predicted evolutionary track to $z = 1$ assuming the inferred SFR profile (Fig. 3), and the orange line marks the evolutionary track for a model galaxy where the scale length of the SFR density of the core and disc scale as $1/(1 + z)$. The half-mass radius at redshifts 5, 3, 2 and 1 is represented by the small squares, indicating that—given the current growth rate—both models predict that this galaxy will evolve onto the size–mass relation of QGs at $z = 2$.
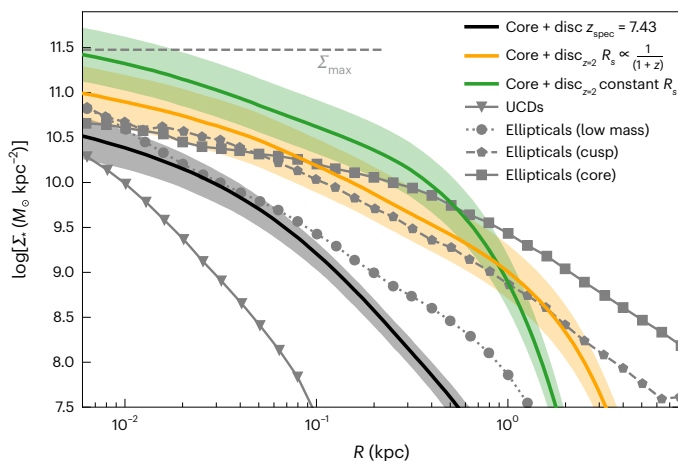
Fig. 5 | Stellar mass surface density profile compared with local galaxies. Radial profiles of stellar mass surface density ($\Sigma_\star$) of JADES-GS+53.18343–27.79097 at $z_{spec} = 7.43$ (black line with shaded region corresponding to 16th and 84th percentiles) compared with average $z = 0$ stellar mass density profiles of UCDs (grey line with triangles), low-mass ellipticals (grey dotted lines with points) and high-mass ellipticals (with core or cusp as a solid line with squares and a dashed line with squares, respectively)[59]. We find that this galaxy is extremely compact: the stellar mass density is consistent within 0.2–0.3 dex of today's massive ellipticals in the central region, while it is a factor of a 1,000 lower in total stellar mass. Also overplotted are the extrapolated profiles at $z = 2$, with the constant SFR scale length (R_s) model in green and the $R_s \propto \frac{1}{1+z}$ model in orange. We see that the redshift-dependent scale model appears more reasonable compared with the redshift 0 ellipticals.

demonstrates the importance of understanding the nature of these earliest systems on spatially resolved scales.

Methods
NIRCam imaging data
We use photometric and spectroscopic data obtained by JWST as part of the JADES[43] collaboration. JADES consists of the NIRCam[46] and

NIRSpec[48] Guaranteed Time Observations instrument teams, and was established to be able to use a combination of imaging and spectroscopy to utilize the full capabilities of both instruments. We use the JADES NIRCam imaging of the GOODS-S field[64]. This consists of imaging in the F090W, F115W, F150W and F200W short-wavelength bands, and the F277W, F335M, F356W, F410M and F444W long-wavelength bands.

The details of the data reduction of the NIRCam data will be presented as part of the JADES programme in S.T. et al. (manuscript in preparation), and have already been described in some detail in refs. 44,65. Briefly, we use the JWST Calibration Pipeline v1.9.2 with the CRDS pipeline mapping (pmap) context 1039. We run Stage 1 and Stage 2 of the pipeline with the default parameters, but provide our own sky-flat for the flat-fielding. Following Stage 2, we perform several custom corrections to account for several features in the NIRCam images[66], including the $1/f$ noise[67], scattered-light effects ('wisps') and the large-scale background. As all of those effects are additive, we fit and subtract them.

Before constructing the final mosaic, we perform an astrometric alignment using a custom version of JWST TweakReg. We calculate both the relative and absolute astrometric correction for images grouped by visit and band by matching sources to a reference catalogue constructed from Hubble Space Telescope (HST) F814W and F160W mosaics in the GOODS-S field with astrometry tied to Gaia Early Data Release 3[68]. We achieve an overall good alignment with relative offsets between bands of less than 0.1 short-wavelength pixel (<3 mas). We then run Stage 3 of the JWST pipeline, combining all exposures of a given filter and a given visit.

NIRSpec spectroscopic data
We used the NIRSpec MSA, with two disperser/filter combinations: PRISM/CLEAR from programme 1180 (hereafter, R100; covers the entire wavelength range $0.7 < \lambda < 5.3$ μm with spectral resolution $R = 30$–100) and the high-resolution grating G395H/F290LP from programme 1286 (hereafter, R2700) to cover the region $2.9 < \lambda < 4.2$ μm with resolution $R = 2,700$. The MSA was configured with the 'three-shutter slitlet', creating an effective slit of 0.2 arcsec width and approximately 1.5 arcsec length. The exposure times were 11,292 s (R100) and 8,009 s (R2700).

For a detailed description of the data reduction, we refer to refs. 45,69,70. Here we note that we applied wavelength-dependent path-loss corrections based on modelling JADES-GS+53.18343−27.79097 as a point source, and extracted the spectrum from a 0.5 arcsec box. The final reduced R100 one-dimensional and two-dimensional spectra are shown in Fig. 1.

The redshift estimate is based on the [O III]λ, λ4959,5007 detection in the R2700 spectrum. We obtain z_{spec} = 7.4303 ± 0.0002(random) ± 0.0005(systematic). To measure the emission-line fluxes, we used the R100 data and penalized pixel-fitting (PPXF)[71,72], which models simultaneously the underlying continuum, as described in ref. 70.

Galaxy selection

To model the spatially resolved stellar populations, we selected JADES-GS+53.18343−27.79097 from the JADES GOODS-S imaging region with F335M and F410M medium-band coverage and a spectroscopic redshift. We used spectroscopic redshifts from both JADES and FRESCO[73], focusing on the redshift interval of z = 7.0–7.8, as we wanted to both probe the very earliest galaxies while also having the Balmer break falling within our filters. Out of these (about 20) galaxies, JADES-GS+53.18343−27.79097 appeared to be the most intriguing with evidence of a core–disc structure and colour gradient (Extended Data Fig. 6). We also note that this galaxy was included in the six sources analysed in ref. 51 where they found evidence for rotation likely tracing the disc component.

Due to this selection procedure, we make no claims about population statistics for this type of galaxy at these redshifts, only that it is a fascinating object in its own right. In a future work, we will explore the population statistics for a mass-complete sample of similar (bulge–disc) galaxies. Importantly, this galaxy does not seem to be peculiar given its stellar mass and redshift: it is only slightly above the extrapolated star-forming main sequence[74–78] (Supplementary Fig. 1) and shows the typical emission-line properties for galaxies at this redshift (refer to 'Emission-line properties' and 'Star formation versus AGN'). JADES-GS+53.18343−27.79097 has previously been identified in HST imaging for the GOODS-S field as a Lyman break galaxy at $z ≈ 7$–8 (it is the source UDF-3244-4727 in ref. 79 based on HST-NICMOS and ACS imaging, and was independently selected in subsequent HST/WFC3 imaging as GS.D-YD4 in ref. 80).

Extended Data Fig. 6 shows images of the galaxy in the F277W band (top-left panel), the F356W band (top-middle panel), the F410M band (top-right panel), and the PSF-matched radial profiles of the F356W–F410M and F277W–F356W colour (bottom panel). The radial colour profile is computed from the PSF-matched images (PSF-matched to F444W) to remove gradient effects resulting from the wavelength-dependent PSF. Interestingly, we find opposite trends for the two colours: the F356W–F410M colour gets redder towards the outskirts, while the F277W–F356W colour gets bluer. As the F356W–F410M colour traces mainly the emission-line excess ([O III] and Hβ lines), we find that those emission lines become more prominent towards the outskirts. Howeve, the F277W–F356W colour traces the rest-frame 4,000 Å spectral region, implying that the centre shows a Balmer/4,000 Å break, while the outskirts show a Balmer jump. This indicates that the outskirts have a younger stellar population than the central region. Interestingly, the ionized gas of JADES-GS+53.18343−27.79097 is actually consistent with a rotationally supported component with $v(r_{eff})/\sigma_0 ≈ 1.3$, as recently shown in ref. 51.

Morphology and photometry with ForcePho

It is challenging to assess the morphology and spatially resolved stellar populations of galaxies at $z > 3$ because (1) they are compact with typical sizes of 0.1–0.4 arcsec, that is, of the order of size of the NIRCam/F200W PSF, and (2) the NIRCam PSF full-width at half-maximum varies by a factor 4 from the bluest (F115W) to the reddest (F444W) band. Given this variation in the PSF full-width at half-maximum, there are two

routes to analysing the data: (1) performing pixel-by-pixel SED fitting on images convolved to the F444W resolution, or (2) modelling the galaxy's deconvolved light distribution in each band independently. Convolving to F444W resolution would lose the high spatial resolution available to us in the blue bands, which provides crucial insights into the morphology of the source; therefore, we choose to forward-model the galaxy's light distribution. Importantly, the observed colour gradient is not caused by the PSF as we show in Extended Data Fig. 6 after homogenizing for the PSF, the colour gradient is still present. This implies that there is an intrinsic colour gradient. To model the intrinsic colour gradient, we have to vary the structural components of the galaxies as a function of wavelength (just changing the normalization will not be enough because the radial component will cancel out in the colour term). This can be done via: (1) fitting an individual Sérsic profile with wavelength-dependent size and/or Sérsic index; or (2) fitting a two-component Sérsic model with fixed size and Sérsic index, but wavelength-dependent normalization. We chose option 2 because it has a stronger physical motivation. A given physical component (bulge, disc or clump) has a certain morphology (size and shape) and stellar population properties (stellar mass, SFH and so on). This means that a component has a certain SED, that is, the flux changes as a function of wavelength, but the shape remains the same. Furthermore, fixing the shape parameters will allow the use of the full signal-to-noise ratio across all bands.

A challenge with this approach is that we have to choose a parametric model that describes the galaxy well. As outlined below ('Motivation for the multiple-component fit'), we experimented with different models, finding that two central components with a clump in the outskirts are able to reproduce the light distribution of JADES-GS+53.18343−27.79097 in all bands the best (both visually and quantitatively (Supplementary Fig. 2). Our main aim here is to describe the stellar populations on spatially resolved scales (Fig. 4), while the physical interpretation of the different components is of secondary importance, but remains of interest given the insights into bulge–disc systems at lower redshifts[18,29,30].

We choose here to forward-model the light distribution in all nine NIRCam images using ForcePho (B.J.D. et al., manuscript in preparation). ForcePho fits multiple PSF-convolved Sérsic profiles simultaneously to all individual exposures and filters by sampling the joint posterior distribution via Markov chain Monte Carlo. This allows us to take into account and measure the covariances between all the parameters. We run ForcePho on the individual NIRCam exposures, which is a key advantage over other codes that run on mosaics, such as galfit[81], lenstronomy[82] or ProFit[83]. First, when the individual cal frame images (Stage 2 products) are co-added to build the final mosaic, information is lost by construction. Working therefore on the mosaic means working on data with less information than the full set of individual exposures. This is particularly important for compact objects, such as JADES-GS+53.18343−27.79097. The individual exposures capture these compact objects with several different pixelizations (owing to different dither positions), while the mosaics are a single-pixel representation. Information is also lost about the correlation between pixel fluxes in the mosaics. Second, alternative methods work with ePSFs, which are based on a few stars that are not saturated, leading to substantial uncertainty in the outskirts of the ePSFs due to noisy outskirts of individual stars. Furthermore, the ePSFs are only marginally oversampled, which leads to uncertainties in the convolution. The PSFs of the cal frame images can be well described with WebbPSF[84,85] (see also 'PSF approximations in ForcePho'). Therefore, tools such as ForcePho that can work on individual exposures have a significant advantage over tools that work on mosaics with ePSFs. Furthermore, ForcePho has been successfully applied to modelling multiple components in refs. 44,65,86. As ForcePho needs to perform many convolutions, it works with Gaussian mixture models for both the PSF and the Sérsic profile. The PSF is approximated with four positive Gaussians.

The introduced systematics are investigated in 'PSF approximations in ForcePho' and motivate us to assume an error floor for the parameters estimated by ForcePho (20% for the effective radii and 0.3 for the Sérsic index of the core).

We run ForcePho assuming a three-component model: two central components and one off-centred clump. Our data prefer this three-component model over a more simple model (one- or two-component model), as shown in 'Motivation for the multiple-component fit' both visually and quantitatively. We assume that the structural parameters are constrained by a combination of the bands, while the flux is fit individually in each band. For the two central components, we fit for the centre, the axis ratio, the position angle and the size. The prior on the size is uniform from 0.001″ to 1.0″. Importantly, we fix the Sérsic index n of one of the central components to 1.0 (sampling it from a range of 0.99 to 1.01), while the other central component is allowed to vary between $2 < n < 5$. The motivation for fixing the Sérsic index to 1 for one of the central components comes from restricting the number of degrees of freedom and from lower-redshift observations[18,29], where so-called bulge–disc decomposition fits have been shown to describe well the light and stellar population distributions. The assumption of an exponential disc ($n = 1$) is theoretically motivated as gas that cools in a halo leads to an exponential star-forming disc[4], while observed discs are well fit by an exponential profile[25,26], hence most bulge–disc decomposition studies fix the Sérsic index to 1 (refs. 17,18,30). Furthermore, specifically for this galaxy, ref. 51 shows evidence for rotation in it. Therefore, we call the $n = 1$ component a 'disc', while the second smaller component with $n = 2$–5 is referred to as a 'core'. We fit the off-centred clump as a quasi-point source whose radius is fixed to a maximum of 0.01 arcsec (51 pc) and a fixed Sérsic index of 1 to suppress prominent wings. In total, we fit a model with 43 free parameters and 2 fixed parameters (the Sérsic indices of the disc and the clump).

We check the success of our fits by exploring the overall data, residual and model images (Supplementary Fig. 2, top). Our fit's residuals are generally consistent with the background as can be seen from the imaging, with slight excess residuals seen in the F410M filter probably from the strong emission lines. We find that the best-fit centre of the core and disc align well, with an offset of 0.005″, which is less than 0.2 short-wavelength pixels and less than the size of either central components. The core has a small effective size of 16 ± 3 mas and a Sérsic index of 2.0 ± 0.4, while the disc component has a larger size with 80 ± 16 mas. Supplementary Fig. 3, left, shows the posterior distributions of key parameters from the ForcePho fit (the flux in the F444W and F277W bands and the half-light radius). As can be seen from the corner plot in Supplementary Fig. 3, ForcePho obtained informative posterior distributions for both the central core and the disc components. The Markov chain Monte Carlo approach of ForcePho also allows us to assess the degeneracies in the fitting, as apparent from the covariance in the core and disc fluxes of F444W and F277W. Importantly, the posterior distributions include only the statistical uncertainties and not the systematic effects, and we assume an error floor for both the fitted photometry (of 5%) and for the morphological parameters (20% for the size, and 0.3 for the Sérsic index of the core). This is motivated by the tests described below. In addition, Supplementary Fig. 3, right, shows the ForcePho SEDs of the core, disc and clump components, which indicate different stellar populations for the three different components.

We also test leaving the Sérsic index of the disc free to vary from 0.7 to 1.3, allowing for a broader range of values. We find that we obtain a disc with half-light radii of 0.12″ (±0.02) where the Sérsic index becomes 0.75 (±0.30). Although this is broadly consistent with our fiducial run (2σ), we note that this run is close to the prior boundary, which cannot be extended to lower Sérsic indices due to the Gaussian mixture approach of ForcePho. We acknowledge that a lower Sérsic index might be preferred by the data. Because of the degeneracy of the Sérsic index and size, this run also implies larger sizes, which would only strengthen

our results, where the star-forming disc is more extended than the core of the galaxy. Finally, we check the χ^2 value of this run, finding a value of 0.17 and a reduced χ^2 value of 8.5. This is larger than our fiducial fixed Sérsic component run, which is still the preferred model and includes fewer degrees of freedom.

As shown in 'Motivation for the multiple-component fit', both visually and quantitatively, two central components reproduce the observed light distribution of JADES-GS+53.18343−27.79097. But what is the evidence for calling the two central components 'disc' and 'core'? First, focusing on the structure, we find that the effective size of the disc is over four times larger than the core, which indicates that the core is a much more compact component than the disc. The Sérsic index of the core is consistent with a 'pseudobulge' component (2.0 ± 0.4), that is, we do not find any evidence for a classical bulge-like component. Importantly, we stress that our disc and core are photometric components, and we cannot say anything about the kinematics of those components from our analysis. However, as mentioned above, the ionized gas of JADES-GS+53.18343−27.79097 is actually consistent with a rotationally supported component with $v(r_{eff})/\sigma_0 \approx 1.3$, as recently shown in ref. 51, which motivates us to refer to the extended component as a 'disc'. The resulting SEDs of the core and disc components are shown in the right panel of Supplementary Fig. 3. These SEDs lead to different stellar populations for the core and the disc (see 'SED fitting with Prospector'), consistent with the idea of a slightly older core and a younger disc component. In summary, on the basis of the structure and the inferred SEDs and stellar populations, we find support for interpreting the two central components as a disc and a core.

We find a consistent interpretation from the direct colour analysis presented in 'Galaxy selection' and Extended Data Fig. 6. The F277W−F356W and the F356W−F410M colour profiles indicate an outskirt that is dominated by younger stellar populations than the central region. A direct comparison with the core and disc colour obtained from ForcePho should be taken with a grain of salt, because our decomposition allows for mixing of the different components at fixed radius. We perform aperture photometry on the PSF-matched mosaics using a central aperture of 0.2″ and an outskirt aperture of 0.4″. We find that the colours for the centre are similar to that of the core although with larger differences in the medium bands probably stemming from emission lines (F277W−F356W = $0.15^{+0.07}_{-0.07}$ mag, F356W−F410M = $0.09^{+0.30}_{-0.17}$ mag for the core and F277W−F356W = -0.06 ± 0.06 mag, F356W−F410M = 1.03 ± 0.05 mag for the centre), while the colours for the outskirts are similar to that of the disc (F277W−F356W = $-0.06^{+0.06}_{-0.06}$ mag, F356W−F410M = $1.41^{+0.11}_{-0.05}$ mag for the disc and F277W−F356W = -0.19 ± 0.14 mag, F356W−F410M = 1.07 ± 0.14 mag for the outskirts).

Motivation for the multiple-component fit

It is crucial to check whether a multi-component fit is warranted by the NIRCam imaging data. Part of our motivation for a multiple-component fit is due to an expectation that the normalization of different components will vary as a function of wavelength; therefore, the structure will also vary with wavelength. One example of this is to fit the short-wavelength and long-wavelength bands separately. We find that the long-wavelength bands fit is broadly consistent with the fiducial run ($r_{half} = 0.028″$) for the core and 0.088″ for the disc, while the short-wavelength fit inverts the radii of the core and disc components 0.042″ and 0.029″ respectively. We would expect the long-wavelength data to best mirror the fiducial run as we have more possible exposures in this wavelength range, while for the short-wavelength bands we are relying on only the exposures from four filters, hence the obvious degeneracies between the components. Supplementary Fig. 2, top, shows the data, the residual and the best-fit model for the three-component fit in all the JADES filters. We see that we can reproduce the observed light distribution in each filter for this three-component model. We then compare this with two simpler

models. We incorporate a χ^2 measure for the ForcePho fits, where we measure the χ values of all pixels within a segmentation map image of the galaxy, as calculated from the F444W image. We then calculate the χ^2 value as the sum of the residuals of all stacked pixels within the segmentation map divided by the noise (estimated from the background). The reason we use a segmentation map is twofold: first, we do not want the metric to be dependent on the size of the cutout, and second, if we included all pixels in the cutout we would be dominated by the background pixels rather than pixels within the galaxy. We find that for the three-component model, this gives us a χ^2 value of 0.14. We note that the exact values depend on the exact choice of the segmentation map.

We run a single-component fit as a comparison with the three-component model. This means that we treat the whole galaxy as a single component and allow its Sérsic index to vary freely from 0.8 to 6, enabling it to be modelled as a disc or bulge-like component. As can be seen in Supplementary Fig. 2, bottom, we find that the one-component fit (bottom panel) under subtracts the central region (that is, the core) compared with the three-component fit (top panel); it also significantly fails to fit the clump. The single-component fit gives a χ^2 value of 0.45 indicating that it has struggled more than the three-component run to reproduce the observed light distribution. Our next test is to run a single-component fit for the main galaxy plus the clump (to test whether the core–disc fit is warranted). Once again, the model fails to account for the flux in both the centre and the outskirts, as seen in the top-middle panel in Supplementary Fig. 2 compared with the three-component fit in the top panel. This fit gives a χ^2 value of 0.18, showing an improvement over the single-component fit, but it still does not reproduce the observed light distribution as well as the three-component fit.

We also test the effect of ignoring the clump by fitting for just the core and disc components. The most significant change is that this extends the half-light radius of the disc component from 80 mas to 129 mas, while increasing the core radius to 0.039 mas; in essence, the components expand in radii to try to fit light from the clump. The Sérsic index of the core becomes 2.31. Importantly, we find consistent fluxes for the core and disc components compared with the three-component analysis: changes are well within the uncertainties. Specifically, the core fluxes change less than 10% in all bands except F410M and F444W, for which the fluxes increase by 26% and 25%, respectively. As the disc fluxes for those bands remain unchanged (changes of less than 3%), this indicates that the core picks up clump long-wavelength light. We find a χ^2 value of 0.25 for the fit showing the importance of modelling the clump component. In summary, this test shows that our main results regarding the stellar population differences between disc and core still hold when ignoring the off-centred clump.

In addition to the χ^2 values mentioned above, we also test metrics for goodness of fit that can incorporate the number of degrees of freedom. This is an important consideration, as the χ^2 value alone, while informing us which model best reproduces the data, cannot tell us whether it is worth the increased complexity of the model. However, determining a reduced χ^2 is not trivial in this case because ForcePho does not optimize the total χ^2 itself, but rather fits the individual exposures. As with the aforementioned χ^2, we consider only the pixels within the segmentation map. Our reduced χ^2 is the previously measured χ^2 multiplied by the degrees of freedom. We define the degrees of freedom as the number of independent pixels within the segmentation map minus the number of parameters of the model. The number of independent pixels within the segmentation map is selected as the total number of pixels in the map minus the number of pixels within the full-width at half-maximum of the PSF. The number of model parameters are the free parameters within the fitting for the different component fits. For the three-component core + disc + clump fit, we obtain a reduced χ^2 value of 6.7. For the two-component galaxy + clump fit, we obtain a value of 11.4. The two-component core + disc fit gives a value of 15.7 and the single-component galaxy gives 35.2. In summary, even after

considering the degrees of freedom, our fiducial three-component core + disc + clump has the smallest reduced χ^2 value.

PSF approximations in ForcePho

ForcePho approximates the JWST PSFs with a Gaussian mixture model. Four Gaussians are able to describe the key components of the JWST/NIRCam PSFs as provided by WebbPSF. In this section, we explore the validity of these PSF approximations specifically for the data and JADES-GS+53.18343−27.79097 presented in this work.

We simulate the best-fit three-component model ('Morphology and photometry with ForcePho') with Galsim[87]. Specifically, we produce the full set of Stage 2 products as given by our observations, assuming the best-fit three-component model for our galaxy and PSFs directly obtained from WebbPSF. We then refit with a three-component model with ForcePho, assuming the same set-up as described above. Supplementary Fig. 4 shows the recovery of the core-to-total (C/T) ratio as a function of the filter wavelength (left panel) and the half-light radius versus the F277W flux for the three components (right panel), with the contours corresponding to the posteriors and the black point is the input value. We are able to recover to within 1σ the C/T ratio, but all wavelengths are biased high, that is, the recovered cores are overestimated relative to the discs. We find that the C/T ratios at all wavelengths are biased high, that is, the recovered cores are overestimated relative to the discs. Although we can recover the C/T ratios within 1σ, this clearly shows a bias on the level of 5–10%. It is comforting that this bias is nearly wavelength independent (variations within <5%), which implies that only the normalization of the SED of the core and the disc are affected, but not their colours. This in turn means that we possibly overestimate the stellar mass of the core by 5% relative to the disc. The right-hand plot of Supplementary Fig. 4 shows that we are able to recover the morphological parameters (that is, half-light size) well, within 0.05 dex (10–20%). To account for possible systematics, we assume an error floor of 20% for the measured sizes, that is, inflate the uncertainties if necessary.

This test leaves open whether WebbPSF provides accurate PSFs. We have tested this in detail in ref. 88 by constructing and comparing empirical PSFs both from true observed stars (called ePSFs) and from WebbPSF point sources injected at the Stage 2 level images (called model PSFs (mPSFs)). Specifically, we construct ePSFs using the empirical method proposed by ref. 89. This method solves the centroids and fluxes of a list of input point sources, and then stacks all the point sources together to get the ePSF. For the list of point sources, we visually identified a sample of 15 isolated point sources from JADES, which are bright but unsaturated. We obtain mPSFs by injecting WebbPSF-based PSFs into the Stage 2 images and then mosaicking them in the same way as our normal mosaics, producing 'star' images. We have then constructed mPSFs from those star images in the same way as the ePSFs. Importantly, we find excellent agreement between ePSF and mPSF, with a typical difference ≲1% in the radial profile of enclosed energy, from the central pixel out to 3 arcsec. This implies that the prediction of WebbPSF is accurate.

SED fitting with Prospector

Prospector[52] is an SED-fitting code that takes in photometric fluxes and flux errors and fits model SEDs to them. It uses the dynamic nested sampling package Dynesty[90] and models the stellar populations via flexible stellar population synthesis (FSPS)[91,92], where we use mesa isochrones and stellar tracks (MIST)[93] and a Chabrier[94] initial mass function.

We assume a stellar population model similar to that in ref. 95. Briefly, we assume a flexible SFH with 6 different time bins, where the most recent bin covers the past 5 Myr, with the other bins being split between 5 Myr and 520 Myr ($z = 20$) in log steps. We use the standard continuity prior[53], which weights against a bursty SFH. We use a top-hat prior on the log stellar mass, where it varies from 6 to 12. To model

the effect of dust attenuation we use a flexible two-component dust model[96], which models a separate birth cloud component (attenuating emission from gas and stars formed in the past 10 Myr) and a diffuse component (attenuating all emission from the galaxy). We use a joint prior on the ratio between the two dust components, where the prior is a clipped normal between 0 and 2, with a mean of 1.0 and a standard deviation of 0.3. The prior on τ_V, the optical depth of the diffuse component in the V band, is a clipped normal ranging from 0 to 4 with a mean of 0.3 and a standard deviation of 1. The slope of the dust attenuation law of the diffuse component is a free parameter and is modelled as a power law multiplication of the standard[97] law (with a top-hat prior from −1 to 0.4). We also use a top-hat prior for the log stellar metallicity with a minimum of −2.0 and a maximum of 0.19. For the nebular component, managed by FSPS, we have a freely varying ionization parameter and gas-phase metallicity[98].

Supplementary Figs. 5 and 6 and Extended Data Fig. 7 show the corner plots for each component for the stellar mass, sSFR, optical depth of the diffuse component, stellar age (lookback time at which 50% of the stellar mass was formed) and stellar metallicity. The SFHs are shown on the top right. Despite not fully breaking the dust–age–metallicity degeneracy, we are able to constrain the stellar mass and overall SFH well.

To explore the dependency of our results on the SFH prior, we also tried the bursty-continuity prior[99], which enables the SFH to change more rapidly, enabling a more variable (that is, bursty) SFH. In the bursty-continuity prior case, we obtain stellar masses of $\log(M_\star/M_\odot) = 8.49^{+0.22}_{-0.35}$, $\log(M_\star/M_\odot) = 7.75^{+0.18}_{-0.09}$ and $\log(M_\star/M_\odot) = 6.89^{+0.37}_{-0.14}$ for the core, disc and clump components, respectively, compared with $\log(M_\star/M_\odot) = 8.48^{+0.16}_{-0.21}$, $\log(M_\star/M_\odot) = 8.05^{+0.23}_{-0.29}$ and $\log(M_\star/M_\odot) = 7.29^{+0.34}_{-0.36}$ in the standard continuity prior case. Therefore, the stellar masses obtained in both cases are consistent within the errors, suggesting that the stellar masses obtained based on the standard continuity prior are not biased by failing to account for particularly bursty SFHs.

SED fitting of the combined photometry

To assess how this galaxy relates to other galaxies, we need to infer the global stellar populations parameters from the combined photometry, that is, treating the core, disc and clump as a single SED. The combined SED can be seen in the top panel of Supplementary Fig. 7, while the bottom panel shows the corner plot with the SFH inset.

We obtain a stellar mass of $\log(M_\star/M_\odot) = 8.44^{+0.22}_{-0.26}$ and $SFR_{10Myr} = 6.3^{+1.6}_{-1.1} M_\odot \, yr^{-1}$ and an sSFR of $\log(sSFR \, yr^{-1}) = -7.56^{+0.31}_{-0.25} \, yr^{-1}$. For comparison, the combined stellar masses of the individual components is $\log(M_\star/M_\odot) = 8.65^{+0.25}_{-0.30}$, while the SFR amounts to $SFR_{10Myr} = 11.5^{+5.7}_{-4.3} M_\odot \, yr^{-1}$. This means that the results are consistent within the uncertainties quoted. We show the results of fitting this combined photometry in Fig. 1 as the orange marker. We see that it is consistent with the black marker (the results of adding the stellar masses and SFRs of the core and disc components). In summary, we find that this galaxy increases its SFH, as expected for galaxies at this epoch.

The clump component

In this section, we explore the clump component seen in the imaging data and modelled as a point source. Supplementary Fig. 8, left, shows the RGB image of the galaxy with the position of the clump highlighted. The clump itself does not fall into the NIRSpec slit, so it is natural to wonder whether it is actually at the same redshift as the core–disc components. On the basis of the RGB image, it appears to have similar colours, suggesting that this is likely. To quantify this further, we determine a photometric redshift by running Prospector on the ForcePho photometry with redshift left as a free parameter with a top-hat prior varying from 0.1 to 13. Supplementary Fig. 8, right, shows the resulting density distribution for the redshift of the clump component.

It appears to be double-peaked, but is consistent with the core and disc component's spectroscopic redshift. This means that it is realistic to consider that the clump is either part of the galaxy (that is, a violent disc instability) or a merging galaxy at the same redshift.

Emission-line properties

The NIRSpec R100 spectrum contains crucial information. However, as outlined above, we include only the inferred redshift as a constraint when performing SED modelling of the morphologically distinct components. The main reason for this is that the spectrum (Fig. 1) covers only parts of the galaxy and includes both core and disc components, but the degree of which is unknown. In principle, one could forward-model the full ForcePho model through the slit, then perform a simultaneous fit of both SED components. Unfortunately, this is not yet possible with the Prospector framework.

Nevertheless, it is important to compare whether the photometry and spectroscopy are consistent with each other and to compare the SED-derived quantities with the ones obtained only from the spectrum. Supplementary Fig. 9 shows the NIRSpec spectrum (black) with synthetic photometry (orange) produced by integrating the flux from the spectrum within each filter. The observed photometry for the core (red) component, the disc (blue), and the combined core + disc galaxy (lilac) is overplotted. The key comparison here is with the combined photometry (in purple). We see that the synthetic photometry follows the same trends as the combined ForcePho photometry with strong jumps flux in F410M and F444W corresponding to the strong line emission in the galaxy. We use the measured flux from the [O III]λ5007, 4963 doublet and the Hβ emission line from the spectrum to calculate their contribution to the F410M and F444W filters. We find that they account for 46% of the flux in the F410M band and 23% of the flux in F444W, hence both of these bands are being boosted by the emission-line flux. We also see that the overall shape of the synthetic photometry and the actual spectrum mirror the actual photometry with a median χ^2 value of 2.5. If we compare the values of the emission lines from the spectrum to the photometry, we find that they are in good agreement (within 1σ) with values of [O III]λ5007, 4963 = $7.52^{+0.10}_{-0.12}[10^{-18} \, erg \, cm^{-2} \, s]$ and Hβ = $0.91^{+0.11}_{-0.08}[10^{-18} \, erg \, cm^{-2} \, s]$ from the observed NIRSpec spectrum and [O III]λ5007, 4963 = $8.45^{+0.6,86}_{-3.33}[10^{-18} \, erg \, cm^{-2} \, s]$ and Hβ = $1.89^{+0.1,87}_{-0.74}[10^{-18} \, erg \, cm^{-2} \, s]$ for the combined core + disc galaxy from the best-fit photometry.

We infer several important quantities from the emission lines obtained from the NIRSpec R100 prism spectra (Fig. 1, bottom). First, we do the fitting and measure the fluxes ('NIRSpec spectroscopic data'), then we correct the fitted emission lines for extinction using the ratio between the Hγ and Hβ Balmer lines (as in ref. 100). The intrinsic value of the ratio (assuming case B recombination, electron temperature $T_e = 1.5 \times 10^4$ K and an electron density of $N_e = 300 \, cm^{-3}$) is 0.468. We measure Hγ/Hβ = 0.409, meaning we are seeing the effects of dust. We obtain a dust extinction of $A_{V,gas} = 0.8^{+1.2}_{-0.8}$ mag in the V band. We also note that this dust extinction is also consistent with that obtained from our SED fitting (of only the photometry), where we obtain $A_V = 0.31^{+0.20}_{-0.13}$ mag for the disc.

We calculate the gas-phase metallicity of JADES-GS+53.18343−27.79097 using the strong line method (for example, refs. 101–105), which uses the ratios of strong emission lines, in this case [O III]λ5007, [O II]λ3727, Hβ and [Ne III]λ3969. We use the strong line metallicity diagnostics from ref. 102.

We obtain a gas-phase metallicity of 12 + log(O/H) = $7.86^{+0.09}_{-0.09}$, which is broadly consistent with that of other galaxies at these redshifts[106]. This is equivalent to a gas-phase metallicity (in units of solar metallicity) of $\log(Z_{gas}/Z_\odot) = 0.83$, which is larger than the stellar metallicities inferred for the core and disc from Prospector, but broadly consistent with the average of the gas-phase metallicity inferred for the two with $\log(Z_{gas}/Z_\odot) = -1.46^{+0.72}_{-0.37}$ for the disc and $\log(Z_{gas}/Z_\odot) = -0.955^{+0.54}_{-0.26}$ for the core.

We can calculate an estimate of the SFR from the dust-corrected Hβ emission line by assuming a Balmer decrement flux ratio of $F_{H\alpha}/F_{H\beta} = 2.86$, corresponding to case B recombination at a temperature of $T \approx 10^4$ K (as in refs. [70,107]). This enables us to estimate Hα. We then convert this Hα flux into a Hα luminosity, which we convert into a SFR using the conversion detailed in ref. [108]. This gives us an SFR of $\mathrm{SFR} = 8.5^{+34.7}_{-7.7} \, M_\odot \, \mathrm{yr}^{-1}$. This is consistent with the combined SFR of the core and disc obtained via SED fitting with Prospector where $\mathrm{SFR}_{10\mathrm{Myr}} = 11.5^{+5.7}_{-4.3} \, M_\odot \, \mathrm{yr}^{-1}$.

Star formation versus AGN

Is the central component a stellar core or an AGN? We know that the central component of this galaxy is compact, with a deconvolved half-light radius of about 80 pc and a Sérsic index of 2.0. We use dust-corrected emission-line diagnostics from the NIRSpec spectrum to investigate a possible AGN contribution. We use the ratio [O III]λ5007/Hβ from the classical BPT[109] diagram and find that this gives us a value of ~4.5 (Supplementary Fig. 10), which, while large for the local Universe, is consistent with star-formation at high redshifts[69,110]. Supplementary Fig. 10, left, shows the BPT diagram of [O III]λ5007/Hβ against [N II]λ6584/Hα. As JADES-GS+53.18343−27.79097 has a redshift of 7.43, the [N II]λ6584 and Hα emission lines are shifted out of the NIRSpec wavelength coverage, hence we plot the value of [O III]λ5007/Hβ as a straight red line. We also show the combined data stacks of refs. [69,106]. We overplot contours from local Sloan Digital Sky Survey (SDSS) galaxies with data from ref. [104]. We see that the line ratio for JADES-GS+53.18343−27.79097 appears consistent with those of the stacks for galaxies at similar redshifts, but this itself cannot rule out an AGN contribution (as shown in ref. [111]). Similarly, we do not find indications for strong high-ionization emission lines such as Heλ4686 that cannot be explained by stellar emission. Supplementary Fig. 10, right, shows line fits to the Hβ and [O III] doublet. The key takeaway from this is that we see no broadening of the Hβ line compared with the [O III]. This means JADES-GS+53.18343−27.79097 shows no evidence of being a type-1 AGN.

Overall, this shows that JADES-GS+53.18343−27.79097 appears to be consistent with pure star formation, but we note that it is difficult to fully rule out an AGN.

Data availability

The JADES data are publicly available at https://jades-survey.github.io/scientists/data.html or through the Mikulski Archive for Space Telescopes (MAST) at https://archive.stsci.edu/hlsp/jades. Additional data derived from the raw products are available from the corresponding authors upon reasonable request.

Code availability

AstroPy[112], Prospector[52], Dynesty[90], FSPS[91,92], Galsim[87], WebbPSF and Photutils[113] are all publicly available. ForcePho (B.D.J. et al., manuscript in preparation) is publicly available via GitHub at https://github.com/bd-j/forcepho.

References

1. Bouché, N. et al. The impact of cold gas accretion above a mass floor on galaxy scaling relations. *Astrophys. J.* **718**, 1001–1018 (2010).
2. Dekel, A. & Krumholz, M. R. Steady outflows in giant clumps of high-*z* disc galaxies during migration and growth by accretion. *Mon. Not. R. Astron. Soc.* **432**, 455–467 (2013).
3. Fall, S. M. & Efstathiou, G. Formation and rotation of disc galaxies with haloes. *Mon. Not. R. Astron. Soc.* **193**, 189–206 (1980).
4. Mo, H. J., Mao, S. & White, S. D. M. The formation of galactic discs. *Mon. Not. R. Astron. Soc.* **295**, 319–336 (1998).
5. van den Bosch, F. C. The origin of the density distribution of disc galaxies: a new problem for the standard model of disc formation. *Mon. Not. R. Astron. Soc.* **327**, 1334–1352 (2001).
6. Agertz, O., Teyssier, R. & Moore, B. The formation of disc galaxies in a ΛCDM universe. *Mon. Not. R. Astron. Soc.* **410**, 1391–1408 (2011).
7. Marinacci, F., Pakmor, R. & Springel, V. The formation of disc galaxies in high-resolution moving-mesh cosmological simulations. *Mon. Not. R. Astron. Soc.* **437**, 1750–1775 (2014).
8. Tacchella, S. et al. Evolution of density profiles in high-*z* galaxies: compaction and quenching inside-out. *Mon. Not. R. Astron. Soc.* **458**, 242–263 (2016).
9. Girichidis, P., Naab, T., Hanasz, M. & Walch, S. Cooler and smoother—the impact of cosmic rays on the phase structure of galactic outflows. *Mon. Not. R. Astron. Soc.* **479**, 3042–3067 (2018).
10. Übler, H. et al. Why stellar feedback promotes disc formation in simulated galaxies. *Mon. Not. R. Astron. Soc.* **443**, 2092–2111 (2014).
11. Sales, L. V. et al. Feedback and the structure of simulated galaxies at redshift *z* = 2. *Mon. Not. R. Astron. Soc.* **409**, 1541–1556 (2010).
12. Dutton, A. A. & Van Den Bosch, F. C. The impact of feedback on disc galaxy scaling relations. *Mon. Not. R. Astron. Soc.* **396**, 141–164 (2009).
13. Dubois, Y. et al. The Horizon-AGN simulation: morphological diversity of galaxies promoted by AGN feedback. *Mon. Not. R. Astron. Soc.* **463**, 3948–3964 (2016).
14. Cochrane, R. K. et al. The impact of AGN-driven winds on physical and observable galaxy sizes. *Mon. Not. R. Astron. Soc.* **523**, 2409–2421 (2023).
15. Scannapieco, C. et al. The Aquila comparison project: the effects of feedback and numerical methods on simulations of galaxy formation. *Mon. Not. R. Astron. Soc.* **423**, 1726–1749 (2012).
16. Naab, T. & Ostriker, J. P. Theoretical challenges in galaxy formation. *Annu. Rev. Astron. Astrophys.* **55**, 59–109 (2017).
17. Kormendy, J. & Kennicutt Jr, R. C. Secular evolution and the formation of pseudobulges in disc galaxies. *Annu. Rev. Astron. Astrophys.* **42**, 603–683 (2004).
18. Simard, L., Mendel, J. T., Patton, D. R., Ellison, S. L. & McConnachie, A. W. A catalog of bulge+disc decompositions and updated photometry for 1.12 million galaxies in the Sloan Digital Sky Survey. *Astrophys. J. Suppl. Ser.* **196**, 11 (2011).
19. Hubble, E. P. Extragalactic nebulae. *Astrophys. J.* **64**, 321–369 (1926).
20. Kormendy, J. & Bender, R. A proposed revision of the Hubble sequence for elliptical galaxies. *Astrophys. J. Lett.* **464**, L119 (1996).
21. Willett, K. W. et al. Galaxy Zoo 2: detailed morphological classifications for 304 122 galaxies from the Sloan Digital Sky Survey. *Mon. Not. R. Astron. Soc.* **435**, 2835–2860 (2013).
22. Muñoz-Mateos, J. C. et al. Specific star formation rate profiles in nearby spiral galaxies: quantifying the inside-out formation of discs. *Astrophys. J.* **658**, 1006–1026 (2007).
23. Pezzulli, G., Fraternali, F., Boissier, S. & Muñoz-Mateos, J. C. The instantaneous radial growth rate of stellar discs. *Mon. Not. R. Astron. Soc.* **451**, 2324–2336 (2015).
24. Frankel, N., Sanders, J., Rix, H.-W., Ting, Y.-S. & Ness, M. The inside-out growth of the Galactic Disc. *Astrophys. J.* **884**, 99 (2019).
25. Nelson, E. J. et al. Where stars form: inside-out growth and coherent star formation from HST Hα maps of 3200 galaxies across the main sequence at 0.7 < *z* < 1.5. *Astrophys. J.* **828**, 27 (2016).
26. Belfiore, F. et al. SDSS IV MaNGA—sSFR profiles and the slow quenching of discs in green valley galaxies. *Mon. Not. R. Astron. Soc.* **477**, 3014–3029 (2018).
27. Ellison, S. L. et al. Star formation is boosted (and quenched) from the inside-out: radial star formation profiles from MaNGA. *Mon. Not. R. Astron. Soc.* **474**, 2039–2054 (2018).

28. Madau, P. & Dickinson, M. Cosmic star-formation history. *Annu. Rev. Astron. Astrophys.* **52**, 415–486 (2014).

29. Tacchella, S. et al. SINS/zC-SINF Survey of z ~ 2 galaxy kinematics: rest-frame morphology, structure, and colors from near-infrared Hubble Space Telescope imaging. *Astrophys. J.* **802**, 101 (2015).

30. Lang, P. et al. Bulge growth and quenching since z = 2.5 in CANDELS/3D-HST. *Astrophys. J.* **788**, 11 (2014).

31. Nelson, E. et al. A massive galaxy in its core formation phase three billion years after the Big Bang. *Nature* **513**, 394–397 (2014).

32. Robertson, B. E. Galaxy formation and reionization: key unknowns and expected breakthroughs by the James Webb Space Telescope. *Annu. Rev. Astron. Astrophys.* **60**, 121–158 (2022).

33. Rodriguez-Gomez, V. et al. The merger rate of galaxies in the Illustris simulation: a comparison with observations and semi-empirical models. *Mon. Not. R. Astron. Soc.* **449**, 49–64 (2015).

34. Fakhouri, O., Ma, C.-P. & Boylan-Kolchin, M. The merger rates and mass assembly histories of dark matter haloes in the two Millennium simulations. *Mon. Not. R. Astron. Soc.* **406**, 2267–2278 (2010).

35. Snyder, G. F. et al. Massive close pairs measure rapid galaxy assembly in mergers at high redshift. *Mon. Not. R. Astron. Soc.* **468**, 207–216 (2017).

36. Hernquist, L. Tidal triggering of starbursts and nuclear activity in galaxies. *Nature* **340**, 687–691 (1989).

37. Mihos, J. C. & Hernquist, L. Gas dynamics and starbursts in major mergers. *Astrophys. J.* **464**, 641 (1996).

38. El-Badry, K. et al. Breathing FIRE: how stellar feedback drives radial migration, rapid size fluctuations, and population gradients in low-mass galaxies. *Astrophys. J.* **820**, 131 (2016).

39. Shen, X. et al. The THESAN project: galaxy sizes during the epoch of reionization. Preprint at https://arxiv.org/abs/2402.08717 (2024).

40. Kartaltepe, J. S. et al. CEERS Key Paper. III. The diversity of galaxy structure and morphology at z = 3-9 with JWST. *Astrophys. J. Lett.* **946**, L15 (2023).

41. Suess, K. A. et al. Rest-frame near-infrared sizes of galaxies at cosmic noon: objects in JWST's mirror are smaller than they appeared. *Astrophys. J. Lett.* **937**, L33 (2022).

42. Ferreira, L. et al. The JWST Hubble sequence: the rest-frame optical evolution of galaxy structure at 1.5 < z < 6.5. *Astrophys. J.* **955**, 94 (2023).

43. Eisenstein, D. J. et al. Overview of the JWST Advanced Deep Extragalactic Survey (JADES). Preprint at https://arxiv.org/abs/2306.02465 (2023).

44. Robertson, B. E. et al. Identification and properties of intense star-forming galaxies at redshifts z ≥ 10. *Nat. Astron.* **7**, 611–621 (2023).

45. Curtis-Lake, E. et al. Spectroscopic confirmation of four metal-poor galaxies at z = 10.3–13.2. *Nat. Astron.* **7**, 622–632 (2023).

46. Rieke, M. J. et al. Performance of NIRCam on JWST in flight. *Publ. Astron. Soc. Pac.* **135**, 028001 (2023).

47. Ferruit, P. et al. The Near-Infrared Spectrograph (NIRSpec) on the James Webb Space Telescope. II. Multi-object spectroscopy (MOS). *Astron. Astrophys.* **661**, A81 (2022).

48. Jakobsen, P. et al. The Near-Infrared Spectrograph (NIRSpec) on the James Webb Space Telescope. I. Overview of the instrument and its capabilities. *Astron. Astrophys.* **661**, A80 (2022).

49. Böker, T. et al. In-orbit performance of the Near-infrared Spectrograph NIRSpec on the James Webb Space Telescope. *Publ. Astron. Soc. Pac.* **135**, 038001 (2023).

50. Eisenstein, D. J., Ferruit, P., Rieke, M. J., Willmer, C. N. A. & Willott, C. J. *NIRCam-NIRSpec Galaxy Assembly Survey—GOODS-S—Part #1a* JWST Proposa.l Cycle 1, ID. #1180 (2017).

51. de Graaff, A. et al. Ionised gas kinematics and dynamical masses of z ≳ 6 galaxies from JADES/NIRSpec high-resolution spectroscopy. *Astron. Astrophys.* **684**, A87 (2024).

52. Johnson, B. D., Leja, J., Conroy, C. & Speagle, J. S. Stellar population inference with Prospector. *Astrophys. J. Suppl. Ser.* **254**, 22 (2021).

53. Leja, J., Carnall, A. C., Johnson, B. D., Conroy, C. & Speagle, J. S. How to measure galaxy star formation histories. II. Nonparametric models. *Astrophys. J.* **876**, 3 (2019).

54. Endsley, R. et al. A JWST/NIRCam study of key contributors to reionization: the star-forming and ionizing properties of UV-faint z ~ 7–8 galaxies. *Mon. Not. R. Astron. Soc.* **524**, 2312–2330 (2023).

55. Nelson, E. J. et al. JWST reveals a population of ultrared, flattened galaxies at 2 ≲ z ≲ 6 previously missed by HST. *Astrophys. J. Lett.* **948**, L18 (2023).

56. Williams, C. C. et al. JEMS: a deep medium-band imaging survey in the Hubble Ultra Deep Field with JWST NIRCam and NIRISS. *Astrophys. J. Suppl. Ser.* **268**, 64 (2023).

57. Suess, K. A., Kriek, M., Price, S. H. & Barro, G. Half-mass radii for ~7000 galaxies at 1.0 ≤ z ≤ 2.5: most of the evolution in the mass-size relation is due to color gradients. *Astrophys. J.* **877**, 103 (2019).

58. Norris, M. A. et al. The AIMSS Project—I. Bridging the star cluster-galaxy divide. *Mon. Not. R. Astron. Soc.* **443**, 1151–1172 (2014).

59. Hopkins, P. F., Murray, N., Quataert, E. & Thompson, T. A. A maximum stellar surface density in dense stellar systems. *Mon. Not. R. Astron. Soc.* **401**, L19–L23 (2010).

60. Bezanson, R. et al. The relation between compact, quiescent high-redshift galaxies and massive nearby elliptical galaxies: evidence for hierarchical, inside-out growth. *Astrophys. J.* **697**, 1290–1298 (2009).

61. Oser, L., Naab, T., Ostriker, J. P. & Johansson, P. H. The cosmological size and velocity dispersion evolution of massive early-type galaxies. *Astrophys. J.* **744**, 63 (2012).

62. Zolotov, A. et al. Compaction and quenching of high-z galaxies in cosmological simulations: blue and red nuggets. *Mon. Not. R. Astron. Soc.* **450**, 2327–2353 (2015).

63. Grudić, M. Y., Hopkins, P. F., Quataert, E. & Murray, N. The maximum stellar surface density due to the failure of stellar feedback. *Mon. Not. R. Astron. Soc.* **483**, 5548–5553 (2019).

64. Giavalisco, M. et al. The Great Observatories Origins Deep Survey: initial results from optical and near-infrared imaging. *Astrophys. J. Lett.* **600**, L93–L98 (2004).

65. Tacchella, S. et al. JADES imaging of GN-z11: revealing the morphology and environment of a luminous galaxy 430 Myr after the Big Bang. *Astrophys. J.* **952**, 74 (2023).

66. Rigby, J. R. et al. How dark the sky: the JWST backgrounds. *Publ. Astron. Soc. Pac.* **135**, 048002 (2023).

67. Schlawin, E. et al. JWST noise floor. I. Random error sources in JWST NIRCam time series. *Astron. J.* **160**, 231 (2020).

68. Gaia Collaboration Gaia Early Data Release 3. Summary of the contents and survey properties. *Astron. Astrophys.* **649**, A1 (2021).

69. Cameron, A. J. et al. JADES: probing interstellar medium conditions at z ~ 5.5–9.5 with ultra-deep JWST/NIRSpec spectroscopy. *Astron. Astrophys.* **677**, A115 (2023).

70. Curti, M. et al. JADES: insights on the low-mass end of the mass–metallicity–star-formation rate relation at 3<z<10 from deep JWST/NIRSpec spectroscopy. Preprint at https://arxiv.org/abs/2304.08516 (2023).

71. Cappellari, M. Improving the full spectrum fitting method: accurate convolution with Gauss–Hermite functions. *Mon. Not. R. Astron. Soc.* **466**, 798–811 (2017).

72. Cappellari, M. Full spectrum fitting with photometry in PPXF: stellar population versus dynamical masses, non-parametric star formation history and metallicity for 3200 LEGA-C galaxies at redshift z ≈ 0.8. *Mon. Not. R. Astron. Soc.* **526**, 3273–3300 (2023).

73. Oesch, P. A. et al. The JWST FRESCO survey: legacy NIRCam/grism spectroscopy and imaging in the two GOODS fields. *Mon. Not. R. Astron. Soc.* **525**, 2864–2874 (2023).

74. Brinchmann, J. et al. The physical properties of star-forming galaxies in the low-redshift universe. *Mon. Not. R. Astron. Soc.* **351**, 1151–1179 (2004).

75. Noeske, K. G. et al. Star formation in AEGIS field galaxies since *z*=1.1: the dominance of gradually declining star formation, and the main sequence of star-forming galaxies. *Astrophys. J. Lett.* **660**, L43–L46 (2007).

76. Speagle, J. S., Steinhardt, C. L., Capak, P. L. & Silverman, J. D. A highly consistent framework for the evolution of the star-forming 'main sequence' from *z* ~0–6. *Astrophys. J. Suppl. Ser.* **214**, 15 (2014).

77. Baker, W. M. et al. The molecular gas main sequence and Schmidt–Kennicutt relation are fundamental, the star-forming main sequence is a (useful) byproduct. *Mon. Not. R. Astron. Soc.* **518**, 4767–4781 (2023).

78. Popesso, P. et al. The main sequence of star-forming galaxies across cosmic times. *Mon. Not. R. Astron. Soc.* **519**, 1526–1544 (2023).

79. Bouwens, R. J., Illingworth, G. D., Franx, M. & Ford, H. *z* ~7–10 Galaxies in the HUDF and GOODS fields: UV luminosity functions. *Astrophys. J.* **686**, 230–250 (2008).

80. Lorenzoni, S. et al. Constraining the bright-end of the UV luminosity function for *z* ≈ 7–9 galaxies: results from CANDELS/GOODS-South. *Mon. Not. R. Astron. Soc.* **429**, 150–158 (2013).

81. Peng, C. Y., Ho, L. C., Impey, C. D. & Rix, H.-W. Detailed decomposition of galaxy images. II. Beyond axisymmetric models. *Astron. J.* **139**, 2097–2129 (2010).

82. Birrer, S. & Amara, A. lenstronomy: multi-purpose gravitational lens modelling software package. *Phys. Dark Universe* **22**, 189–201 (2018).

83. Robotham, A. S. G., Taranu, D. S., Tobar, R., Moffett, A. & Driver, S. P. PROFIT: Bayesian profile fitting of galaxy images. *Mon. Not. R. Astron. Soc.* **466**, 1513–1541 (2017).

84. Rigby, J. et al. The science performance of JWST as characterized in commissioning. *Publ. Astron. Soc. Pac.* **135**, 048001 (2023).

85. Perrin, M. D. et al. Updated point spread function simulations for JWST with WebbPSF. In *Space Telescopes and Instrumentation 2014: Optical, Infrared, and Millimeter Wave* Society of Photo-Optical Instrumentation Engineers (SPIE) Conference Series Vol. 9143 (eds Oschmann, J. et al.) 91433X (SPIE, 2014).

86. Tacchella, S. et al. JWST NIRCam+NIRSpec: interstellar medium and stellar populations of young galaxies with rising star formation and evolving gas reservoirs. *Mon. Not. R. Astron. Soc.* **522**, 6236–6249 (2023).

87. Rowe, B. T. P. et al. GALSIM: the modular galaxy image simulation toolkit. *Astron. Comput.* **10**, 121–150 (2015).

88. Ji, Z. et al. JADES + JEMS: a detailed look at the buildup of central stellar cores and suppression of star formation in galaxies at redshifts 3 < *z* < 4.5. Preprint at https://arxiv.org/abs/2305.18518 (2023).

89. Anderson, J. & King, I. R. Toward high-precision astrometry with WFPC2. I. Deriving an accurate point-spread function. *Publ. Astron. Soc. Pac.* **112**, 1360–1382 (2000).

90. Speagle, J. S. DYNESTY: a dynamic nested sampling package for estimating Bayesian posteriors and evidences. *Mon. Not. R. Astron. Soc.* **493**, 3132–3158 (2020).

91. Conroy, C., Gunn, J. E. & White, M. The propagation of uncertainties in stellar population synthesis modeling. I. The relevance of uncertain aspects of stellar evolution and the initial mass function to the derived physical properties of galaxies. *Astrophys. J.* **699**, 486–506 (2009).

92. Conroy, C. & Gunn, J. E. The propagation of uncertainties in stellar population synthesis modeling. III. Model calibration, comparison, and evaluation. *Astrophys. J.* **712**, 833–857 (2010).

93. Choi, J. et al. Mesa isochrones and stellar tracks (MIST). I. Solar-scaled models. *Astrophys. J.* **823**, 102 (2016).

94. Chabrier, G. Galactic stellar and substellar initial mass function. *Publ. Astron. Soc. Pac.* **115**, 763–795 (2003).

95. Tacchella, S. et al. Fast, slow, early, late: quenching massive galaxies at *z* ~ 0.8. *Astrophys. J.* **926**, 134 (2022).

96. Charlot, S. & Fall, S. M. A simple model for the absorption of starlight by dust in galaxies. *Astrophys. J.* **539**, 718–731 (2000).

97. Calzetti, D. et al. The dust content and opacity of actively star-forming galaxies. *Astrophys. J.* **533**, 682–695 (2000).

98. Byler, N., Dalcanton, J. J., Conroy, C. & Johnson, B. D. Nebular continuum and line emission in stellar population synthesis models. *Astrophys. J.* **840**, 44 (2017).

99. Tacchella, S. et al. On the stellar populations of galaxies at *z* = 9–11: the growth of metals and stellar mass at early times. *Astrophys. J.* **927**, 170 (2022).

100. Curti, M. et al. The chemical enrichment in the early Universe as probed by JWST via direct metallicity measurements at *z* ~ 8. *Mon. Not. R. Astron. Soc.* **518**, 425–438 (2023).

101. Curti, M. et al. New fully empirical calibrations of strong-line metallicity indicators in star-forming galaxies. *Mon. Not. R. Astron. Soc.* **465**, 1384–1400 (2017).

102. Bian, F., Kewley, L. J. & Dopita, M. A. "Direct" gas-phase metallicity in local analogs of high-redshift galaxies: empirical metallicity calibrations for high-redshift star-forming galaxies. *Astrophys. J.* **859**, 175 (2018).

103. Curti, M., Mannucci, F., Cresci, G. & Maiolino, R. The mass–metallicity and the fundamental metallicity relation revisited on a fully T_e-based abundance scale for galaxies. *Mon. Not. R. Astron. Soc.* **491**, 944–964 (2020).

104. Baker, W. M. et al. The metallicity's fundamental dependence on both local and global galactic quantities. *Mon. Not. R. Astron. Soc.* **519**, 1149–1170 (2023).

105. Baker, W. M. & Maiolino, R. Stellar mass, not dynamical mass nor gravitational potential, drives the mass-metallicity relationship. *Mon. Not. R. Astron. Soc.* (2023).

106. Sanders, R. L., Shapley, A. E., Topping, M. W., Reddy, N. A. & Brammer, G. B. Direct T_e-based metallicities of *z* = 2–9 galaxies with JWST/NIRSpec: empirical metallicity calibrations applicable from reionization to cosmic noon. *Astrophys. J.* **962**, 24 (2024).

107. Baker, W. M. et al. The ALMaQUEST survey IX: the nature of the resolved star forming main sequence. *Mon. Not. R. Astron. Soc.* **510**, 3622–3628 (2022).

108. Shapley, A. E., Reddy, N. A., Sanders, R. L., Topping, M. W. & Brammer, G. B. JWST/NIRSpec measurements of the relationships between nebular emission-line ratios and stellar mass at *z* ~ 3–6. *Astrophys. J. Lett.* **950**, L1 (2023).

109. Baldwin, J. A., Phillips, M. M. & Terlevich, R. Classification parameters for the emission-line spectra of extragalactic objects. *Publ. Astron. Soc. Pac.* **93**, 5–19 (1981).

110. Shapley, A. E., Sanders, R. L., Reddy, N. A., Topping, M. W. & Brammer, G. B. JWST/NIRSpec Balmer-line measurements of star formation and dust attenuation at z ~ 3–6. *Astrophys. J.* **954**, 157 (2023).

111. Scholtz, J. et al. JADES: a large population of obscured, narrow line AGN at high redshift. Preprint at https://arxiv.org/abs/2311.18731 (2023).

112. Astropy Collaboration The Astropy Project: sustaining and growing a community-oriented open-source project and the latest major release (v5.0) of the core package. *Astrophys. J.* **935**, 167 (2022).

113. Bradley, L. et al. astropy/photutils: 1.6.0. *Zenodo* https://doi.org/10.5281/zenodo.1258523 (2022).

Author contributions

W.M.B. and S.T. led the writing of the paper. W.M.B. performed the analysis (identification of the target, ForcePho fitting, SED modelling and figure making) under the supervision of S.T. and B.D.J. All authors contributed to the interpretation of the results. D.J.E., B.D.J., B.R., S.T., D.P., R.H., Z.J. and C.N.A.W. contributed to the NIRCam imaging reduction. E.N., K.A.S., D.J.E., B.D.J., B.R. and S.T. contributed to the analysis and interpretation of the NIRCam imaging data. F.D'E. contributed to the development of tools for the spectroscopic data analysis. S. Carniani, S. Arribas, M.C. and J.W. contributed to the reduction of NIRSpec data and the development of the NIRSpec pipeline. A.J.B. contributed to the design and optimization of the MSA configurations. F.D'E., M.C., A.d.G., R.M. and J.S. helped with the interpretation of the NIRSpec data.

Competing interests

The authors declare no competing interests.

Additional information

Extended data is available for this paper at https://doi.org/10.1038/s41550-024-02384-8.

Supplementary information The online version contains supplementary material available at https://doi.org/10.1038/s41550-024-02384-8.

Correspondence and requests for materials should be addressed to William M. Baker or Sandro Tacchella.

Peer review information *Nature Astronomy* thanks the anonymous reviewers for their contribution to the peer review of this work.

Reprints and permissions information is available at www.nature.com/reprints.

Publisher's note Springer Nature remains neutral with regard to jurisdictional claims in published maps and institutional affiliations.

¹Kavli Institute for Cosmology, University of Cambridge, Cambridge, UK. ²Cavendish Laboratory - Astrophysics Group, University of Cambridge, Cambridge, UK. ³Center for Astrophysics | Harvard & Smithsonian, Cambridge, MA, USA. ⁴Department for Astrophysical and Planetary Science, University of Colorado, Boulder, CO, USA. ⁵Department of Astronomy and Astrophysics, University of California, Santa Cruz, Santa Cruz, CA, USA. ⁶Kavli Institute for Particle Astrophysics and Cosmology and Department of Physics, Stanford University, Stanford, CA, USA. ⁷European Southern Observatory, Garching bei Muenchen, Germany. ⁸Max-Planck-Institut für Astronomie, Heidelberg, Germany. ⁹Steward Observatory, University of Arizona, Tucson, AZ, USA. ¹⁰Department of Physics and Astronomy, University College London, London, UK. ¹¹Centro de Astrobiología (CAB), CSIC-INTA, Madrid, Spain. ¹²School of Physics, University of Melbourne, Parkville, Victoria, Australia. ¹³ARC Centre of Excellence for All Sky Astrophysics in 3 Dimensions (ASTRO 3D), Melbourne, Victoria, Australia. ¹⁴Department of Physics, University of Oxford, Oxford, UK. ¹⁵Scuola Normale Superiore, Pisa, Italy. ¹⁶Sorbonne Université, CNRS, UMR 7095, Institut d'Astrophysique de Paris, Paris, France. ¹⁷Centre for Astrophysics Research, Department of Physics, Astronomy and Mathematics, University of Hertfordshire, Hatfield, UK. ¹⁸Department of Astronomy, University of Texas, Austin, TX, USA. ¹⁹Department of Physics and Astronomy, The Johns Hopkins University, Baltimore, MD, USA. ²⁰AURA for European Space Agency, Space Telescope Science Institute, Baltimore, MD, USA. ²¹Department of Astronomy, University of Wisconsin-Madison, Madison, WI, USA. ²²NSF's National Optical-Infrared Astronomy Research Laboratory, Tucson, AZ, USA. ✉e-mail: wb308@cam.ac.uk; st578@cam.ac.uk
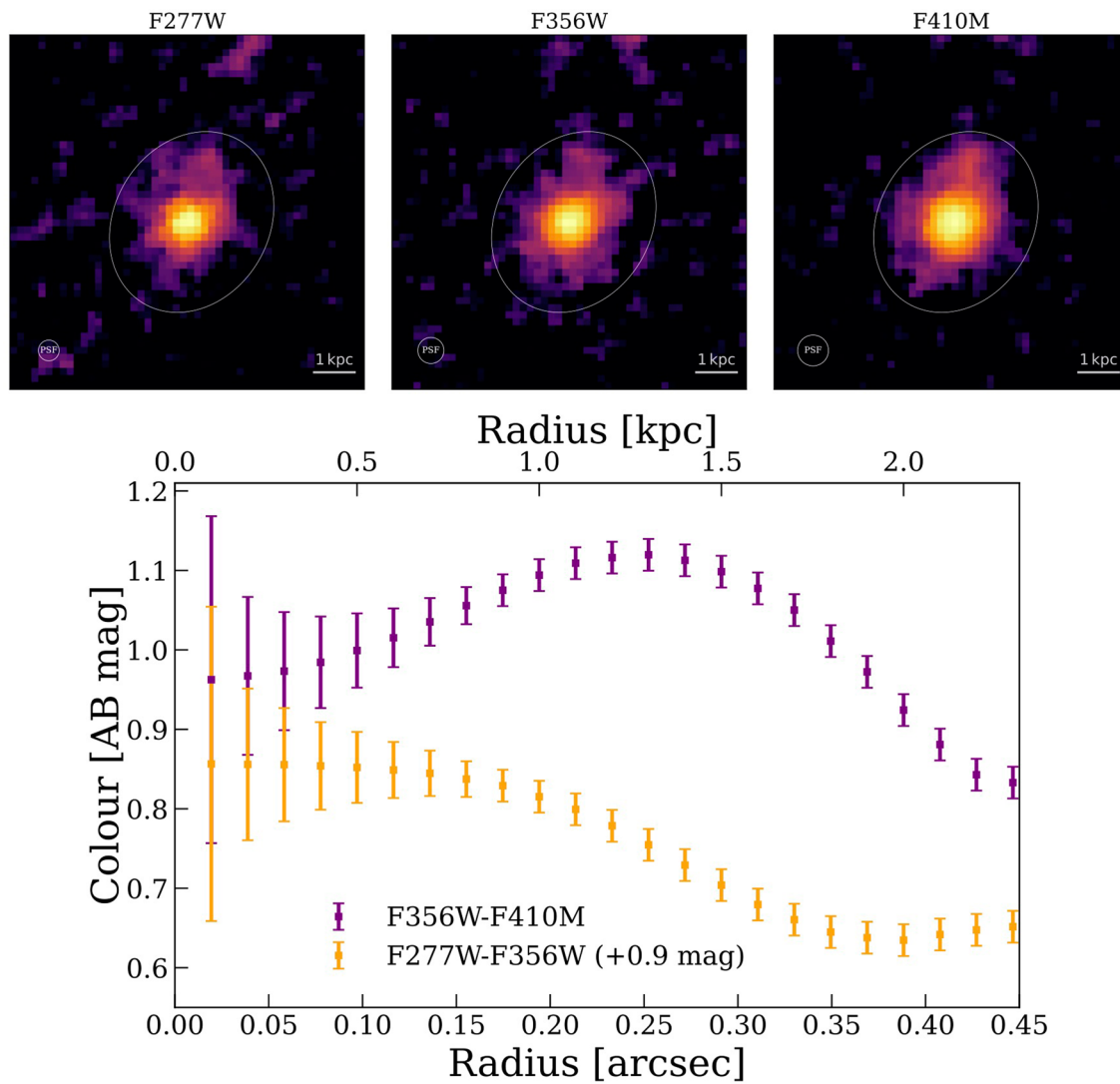
Extended Data Fig. 1 | Colour gradients between the centre and outskirts of the galaxy. Images in the F277W band (upper left panel), F356W band (upper middle panel), F410M band (upper right panel) and the PSF-matched radial profiles of the F356W-F410M and F277W-F356W colour (bottom panel). The size of the FWHM of the PSF (bottom right), a bar indicating 1 kpc at z=7.43 (bottom left) and an elliptical aperture with a major axis length of 0.4 arcsec are shown for reference in each image cutout. The radial colour profile is computed from the PSF-matched images (PSF-matched to F444W) in order to remove gradient effects resulting from the wavelength-dependent PSF. The errors are obtained from the 1σ uncertainty map and propagated forwards. The F277W-F356W is offset by 0.9 mag to highlight the colour gradients seen in the profile. The colour profiles show opposite trends: the F410M excess increases while the F277W-F356W colour (tracing the rest-4000A spectral region) gets bluer toward the outskirts. This indicates that the outskirts – dominated by the disc – has younger stellar population than the central region.
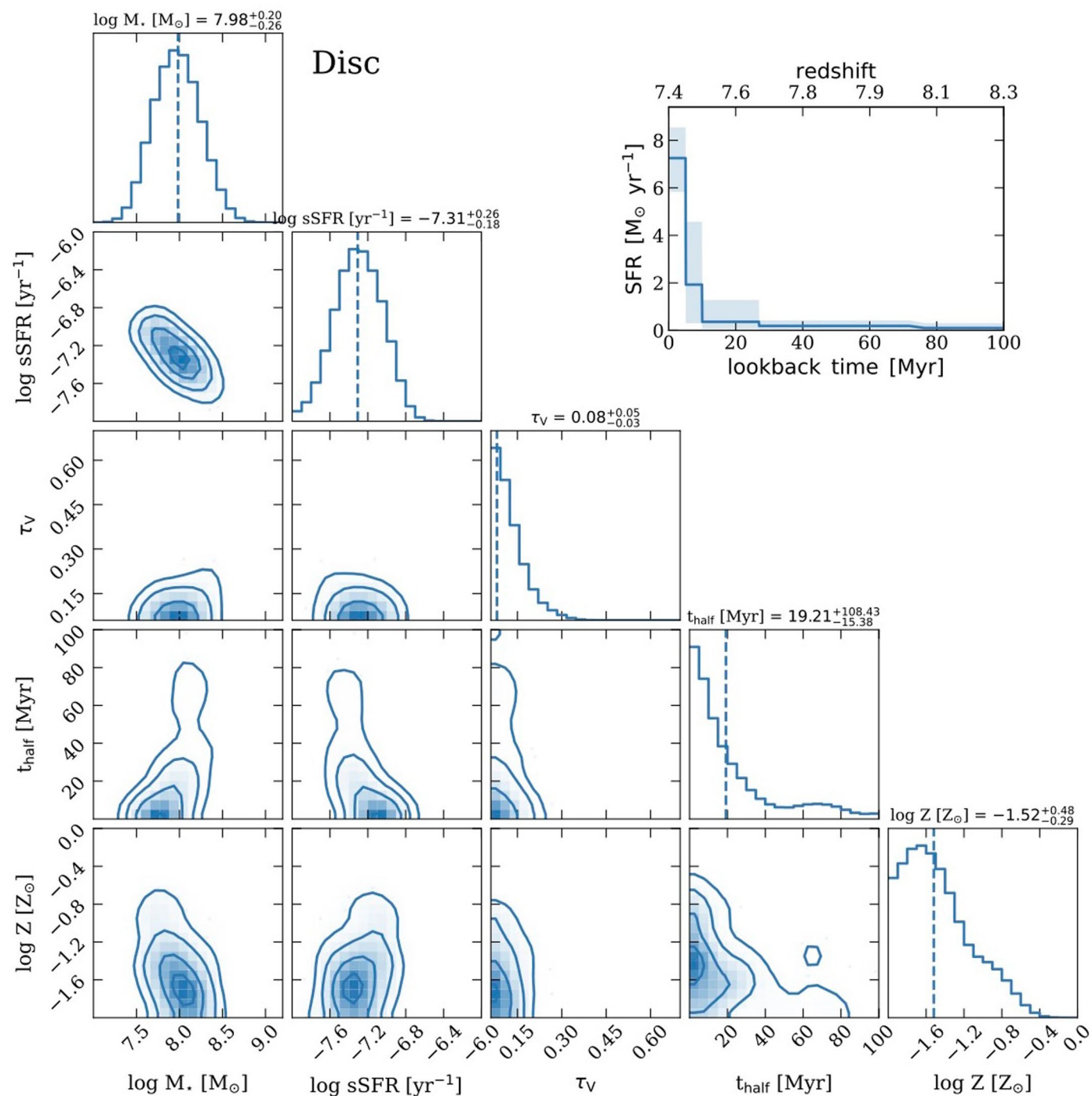
Extended Data Fig. 2 | Corner figure and star-formation history for the disc component. Left: Corner plot showing stellar mass ($M_\star$), specific star-formation rate (sSFR), optical depth (τ_v), half-time (t_{half}) and stellar metallicity (Z) for the disc component as obtained by SED fitting. Right: the SFH for the disc component. The data is presented as the median of the distribution with the errors corresponding to the 16th and 84th percentiles.